Ore Geology Reviews 88 (2017) 768–790

Contents lists available at ScienceDirect

Ore Geology Reviews

journal homepage: www.elsevier.com/locate/oregeorev

Mesozoic multiphase magmatism at the Xinan Cu–Mo ore deposit (Zijinshan Orefield): Geodynamic setting and metallogenic implications

Chao Xu [a,b], Huayong Chen [a,*], Wenting Huang [a,*], Jinping Qi [c], Gan Duan [a,b], Lejun Zhang [d], Chao Wu [a,b], Shuang Zhang [a,b], Wenbiao Zhong [c]

[a] Key Laboratory of Mineralogy and Metallogeny, Guangzhou Institute of Geochemistry, Chinese Academy of Sciences, Guangzhou 510640, PRChina
[b] Graduate University of Chinese Academy of Sciences, Beijing 100049, PR China
[c] Zijin Mining Group Co. Ltd, Shanghang 364200, Fujian, PR China
[d] Centre of Excellence in Ore Deposits (CODES), University of Tasmania, Private Bag 79, Hobart, Australia

ARTICLE INFO

Article history:
Received 27 January 2016
Received in revised form 8 June 2016
Accepted 21 June 2016
Available online 25 June 2016

Keywords:
Xinan Cu–Mo deposit (Zijinshan orefield)
Porphyry–epithermal mineralization
Mesozoic magmatism
Pacific plate subduction
South China

ABSTRACT

The Xinan Cu–Mo deposit, newly-discovered in the Zijinshan Au–Cu–Mo Orefield (the largest porphyry–epithermal system in SE China), is featured by the presence of abundant multi-phase granitoids, which reflects the complex Mesozoic tectono-magmatic evolution in the region.

New and published LA-ICP-MS zircon U–Pb age data reveal that the Mesozoic Zijinshan magmatism occurred in two major phases: (1) Middle to Late Jurassic (ca. 169–150 Ma), forming the Zijinshan complex granite and the Xinan monzogranite; (2) late Early Cretaceous to earliest Late Cretaceous (ca. 112–98 Ma), forming the Shimaoshan volcanic rocks, Sifang granodiorite, and the Xinan (fine-grained) granodiorite porphyry, porphyritic granodiorite and late aplite dykes. Additionally, a possible earliest Cretaceous magmatism (ca. 141 Ma) may have occurred based on inherited zircon evidence. Major and trace element geochemistry indicates that all the Zijinshan igneous rocks show subduction-related geochemical affinities. Zircon Ce^{4+}/Ce^{3+} values of the late Early Cretaceous to earliest Late Cretaceous granitoids ($Ce^{4+}/Ce^{3+} = 190–1706$) are distinctly higher than the Middle to Late Jurassic ones ($Ce^{4+}/Ce^{3+} = 27–457$), suggesting that the former were derived from more oxidized parental magma. The Middle to Late Jurassic Zijinshan complex granite and monzogranite have $\varepsilon_{Hf}(t)$ values of −8.02 to −10.00, with the two-stage Hf model ages (T_{DM2}) of 1.72 to 1.84 Ga (similar to the Paleoproterozoic metamorphosed Cathaysia Block basement), suggesting that they were derived from partial melting of the basement. The late Early Cretaceous to earliest Late Cretaceous Sifang granodiorite and Xinan (fine-grained) granodiorite porphyry, porphyritic granodiorite and aplite dykes contain higher and wider range of $\varepsilon_{Hf}(t)$ values (0.66 to −6.05), with T_{DM2} of 1.12 to 1.56 Ga, indicating that they were also partial melting product of the Cathaysia basement but with more mantle and/or juvenile mafic lower crustal input. We propose that the Zijinshan Orefield was in a compressive, Pacific subduction-related tectonic setting during the Middle to Late Jurassic. The regional tectonic regime may have changed to extensional in the late Early Cretaceous to earliest Late Cretaceous, during which the Pacific plate subduction direction change and the accompanying subduction roll-back and slab window-opening occurred. The tectonic regime transition, high oxygen fugacity and mantle/mafic lower crustal materials involvement in the late Early Cretaceous to earliest Late Cretaceous may have generated the Zijinshan porphyry-related Au–Cu–Mo mineralization.

1. Introduction

Three quarters of the world's Cu, half of the world's Mo and one fifth of the world's Au are currently supplied by porphyry deposits, most of which occur in magmatic arc settings (Cooke et al., 2005; Sillitoe, 2010; Pirajno and Zhou, 2015). The Zijinshan Au–Cu–Mo Orefield is a large porphyry–epithermal system, discovered in the late 1970s in southwestern Fujian, SE China (Zhong, 2014). Porphyry and porphyry-related high-sulfidation epithermal and (minor) intermediate- and low-sulfidation epithermal mineralization were discovered in the orefield (Zhang et al., 1996, 2003; So et al., 1998; Huang et al., 2013; Zhang et al., 2013; Zhong et al., 2014). By the end of 2013, the total proven reserves in the Zijinshan Orefield are 399.82 t Au (0.3 g/t), 4.14 Mt. Cu (0.45%), 6339 t Ag (20 to 156 g/t) and 0.1 Mt. Mo (0.032%) (Zhang, 2013).

* Corresponding authors.
E-mail addresses: huayongchen@gig.ac.cn (H. Chen), wentinghuang@gig.ac.cn (W. Huang).

http://dx.doi.org/10.1016/j.oregeorev.2016.06.019
0169-1368/

Despite decades of research, the magmatic evolution and genetic relationships between magmatism and mineralization at Zijinshan are yet to be well understood, and the Mesozoic tectonic setting at Zijinshan remains controversial (Mao et al., 2002; Yu et al., 2013; Jiang et al., 2013; Li and Jiang, 2014; Zhong, 2014). Zhang et al. (2001) proposed that the Jurassic Zijinshan granitoids were emplaced in a compressive tectonic setting, whereas the Cretaceous granodiorite and volcanic rocks were emplaced in an extensional tectonic setting. Mao et al. (2002) argued that the emplacement of the Jurassic Sifang granodiorite was resulted from asthenospheric upwelling, and some researchers considered that the Cretaceous magmatism occurred in a subduction-related setting (Jiang et al., 2013; Li and Jiang, 2014; Zhong et al., 2014). The newly discovered Xinan Cu–Mo deposit in the Zijinshan Orefield contains multiphase intrusions, which allow us to better understand the Mesozoic tectono-magmatic evolution of the orefield.

In this paper, new and published data on the Xinan (and Zijinshan Orefield) petrography, whole-rock geochemistry, as well as the U–Pb ages, geochemistry and Hf isotopes of zircons were integrated to establish a geodynamic and metallogenic model for the Zijinshan mineral system.

2. Geological background

South China comprises the Yangtze Craton in the northwest and the Cathaysia block in the southeast (Fig. 1A), separated along the Xiang-Gan-Zhe suture (Sengor and Natal'in, 1996; Hsü et al., 1988). The Zijinshan Orefield is situated in the eastern Cathaysia Block (Fig. 1B) at the intersection of the Xuanhe Anticlinorium and Yunxiao-Shanghang Fault (Chen et al., 2011; Zhong et al., 2014). Major lithostratigraphic units include the Neoproterozoic Louziba Group metamorphic rocks, Upper Paleozoic clastic sediments, Early Cretaceous volcanic assemblages and Quaternary alluvial sediments (Fig. 1B) (Wang et al., 2009; Huang, 2014). The Louziba Group comprises low- to medium-grade metamorphosed shallow-marine sediments, including two-

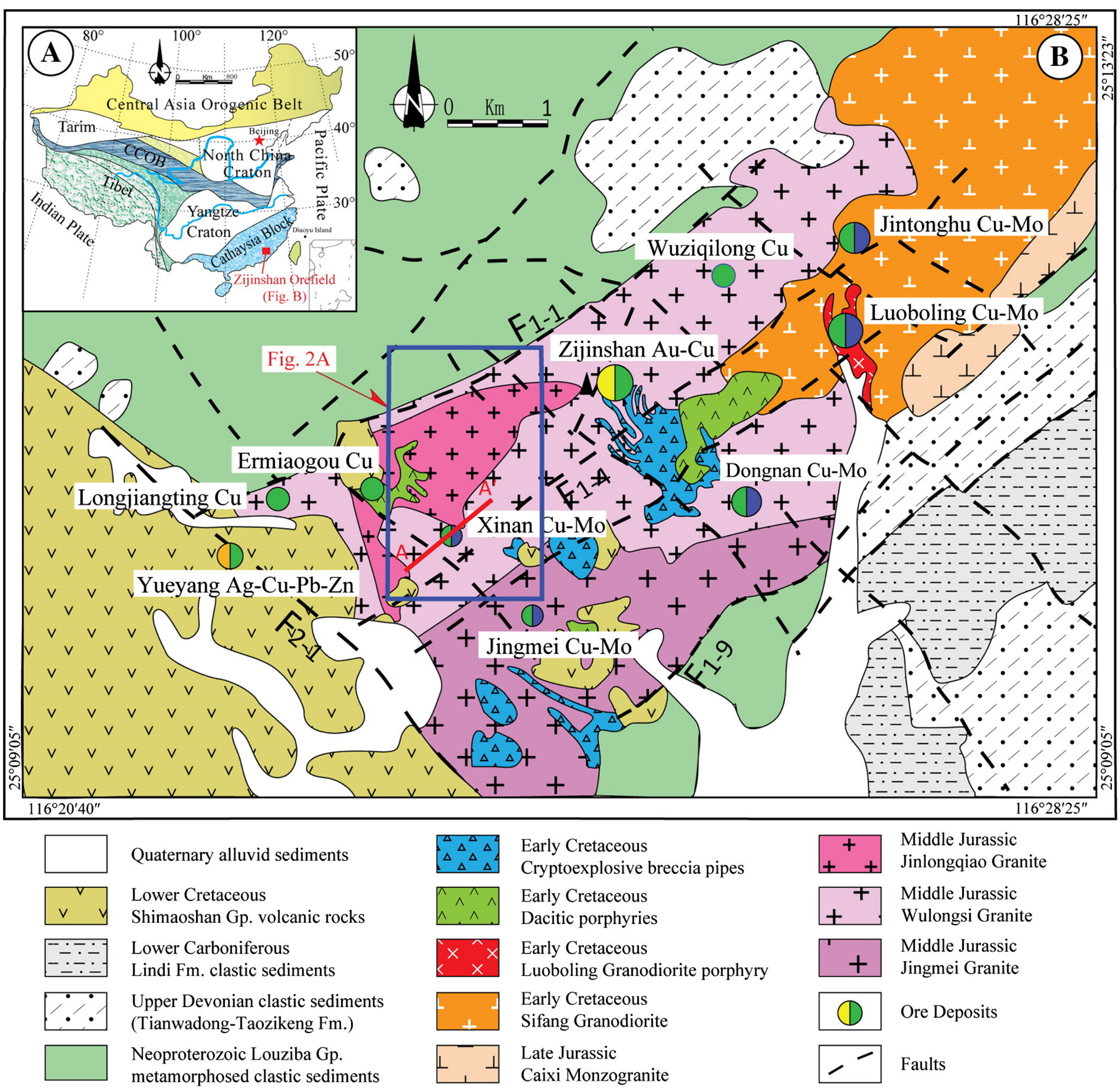

Fig. 1. (A) Tectonic map showing the location of the study area (after Chen et al., 2007). (B) Geological map of the Zijinshan Orefield (modified after Zhong et al., 2014).

mica schist, phyllite and metasandstone. Middle to Upper Paleozoic sedimentary rocks comprise the Upper Devonian Tianwadong and Taozikeng formations and Lower Carboniferous Lindi Formation. These formations comprise coastal to shallow marine siltstone, sandstone and conglomerate, locally intercalated with marl and felsic tuff. The Lower Cretaceous Shimaoshan Group, unconformably overlying the above-mentioned strata, includes dacite, rhyolite, ignimbrite and tuff, with minor conglomerate interbeds (Jiang et al., 2013; Zhong et al., 2014). Major structures at Zijinshan include the NE-trending Xuanhe anticlinorium and NE- and (mineralization-related) NW-trending faults (Zhang et al., 2003; Zhang, 2013) (Fig. 1B).

Middle to Late Jurassic and Early Cretaceous magmatic rocks are widespread at Zijinshan, including the: (1) Middle Jurassic Zijinshan granite complex (ca. 165–155 Ma) in central Zijinshan (Fig. 1B), which contains the Jingmei medium-coarse-grained granite, Wulongsi medium-fine-grained granite and Jinlongqiao fine-grained granite (Zhao et al., 2008; Jiang et al., 2013; Huang, 2014; Li et al., 2015a). (2) Late Jurassic Caixi monzogranite (Fig. 1B) (ca. 155–150 Ma) in northeastern Zijinshan (Zhao et al., 2008; Huang, 2014). (3) Early Cretaceous Sifang granodiorite (ca. 110 Ma) in northeastern Zijinshan, which intruded the Neoproterozoic Louziba Group and the Middle Jurassic Zijinshan granite complex (Fig. 1B) (Jiang et al., 2013; Huang, 2014). (4) Early Cretaceous Luoboling granodiorite porphyry (ca. 107–98 Ma), which intruded the Sifang granodiorite (Fig. 1B) (Huang, 2014; Zhong, 2014). (5) Granitic porphyries, dacite porphyries, cryptoexplosive breccias pipes and late dykes (ca. 108–95 Ma), which intruded the above-mentioned granitoids (Hu et al., 2012; Li et al., 2013; Wu et al., 2013; Jiang et al., 2013; Yu et al., 2013) (Fig. 1B). It is noteworthy that the Luoboling and Xinan granodiorite porphyries show close space-time and genetic relationship with Luoboling and Xinan porphyry Cu–Mo deposit, respectively (So et al., 1998; Zhang et al., 2001; Zhong et al., 2011; Zhong, 2014).

The Xinan Cu–Mo ore deposit (currently explored with identified 0.02 Mt. Cu @ 0.2% and minor Mo) is located to the southwest of the Zijinshan high-sulfidation epithermal Au–Cu deposit (Fig. 1B). Major lithostratigraphic units at the mine include the Neoproterozoic Louziba Group metamorphic rocks and the Early Cretaceous Shimaoshan Group volcanic rocks. The NE- and NW-trending faults controlled the granitoids emplacement, and the latter also controlled the orebody distribution (Fig. 2A). Granitoids at Xinan include the Zijinshan granite complex, monzogranite, (fine-grained) granodiorite porphyry, porphyritic granodiorite and late dykes (e.g., aplite and granite porphyry dykes). Granodiorite porphyry is the major ore-bearing rock (Fig. 2B). From deep to shallow levels, the alteration styles gradate from propylitic, via phyllic, to (advanced) argillic alteration, whereas potassic alteration is not observed. Phyllic alteration is associated with the Cu–Mo mineralization.

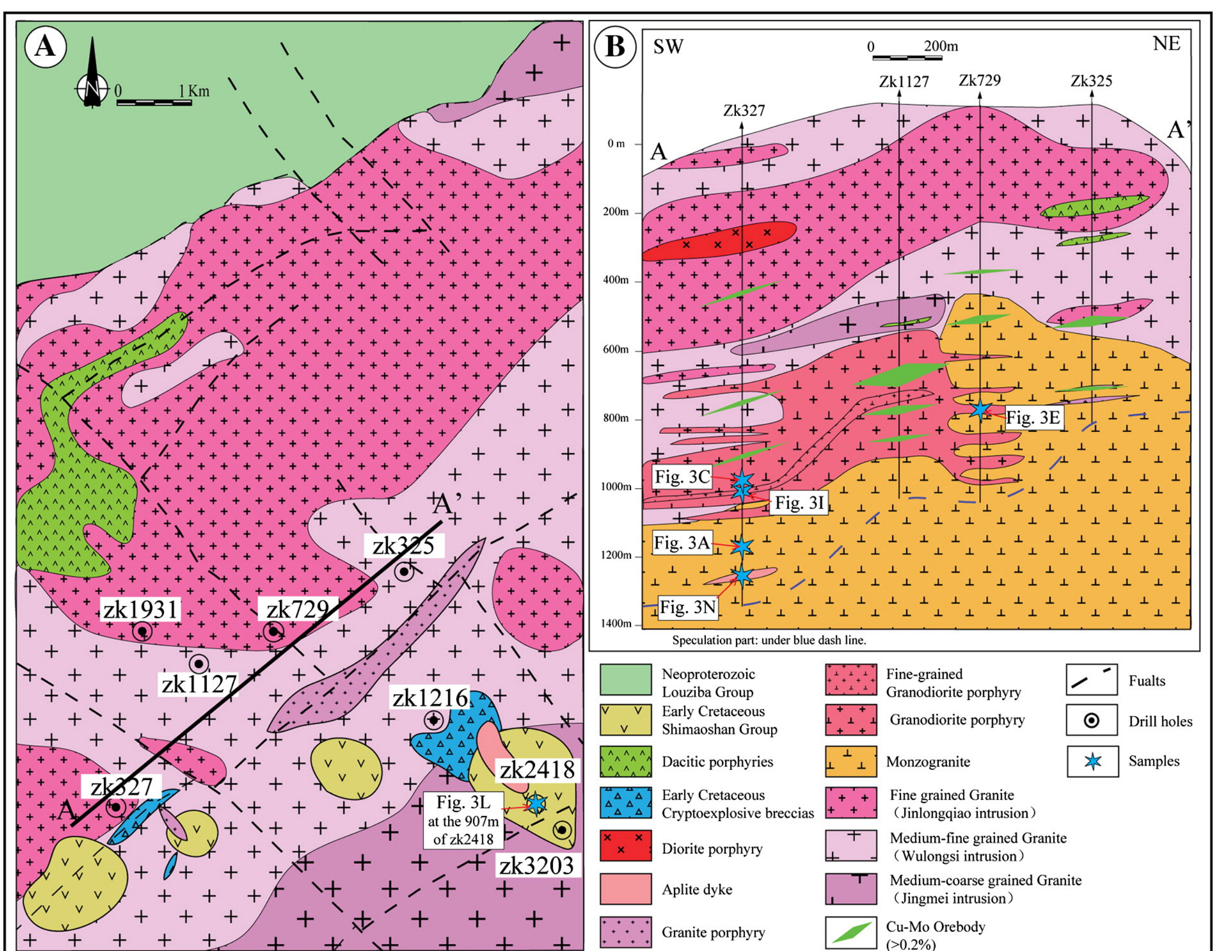

Fig. 2. (A) Geological map of the Xinan Cu–Mo ore deposit and (B) geological profile of NE-trending section.

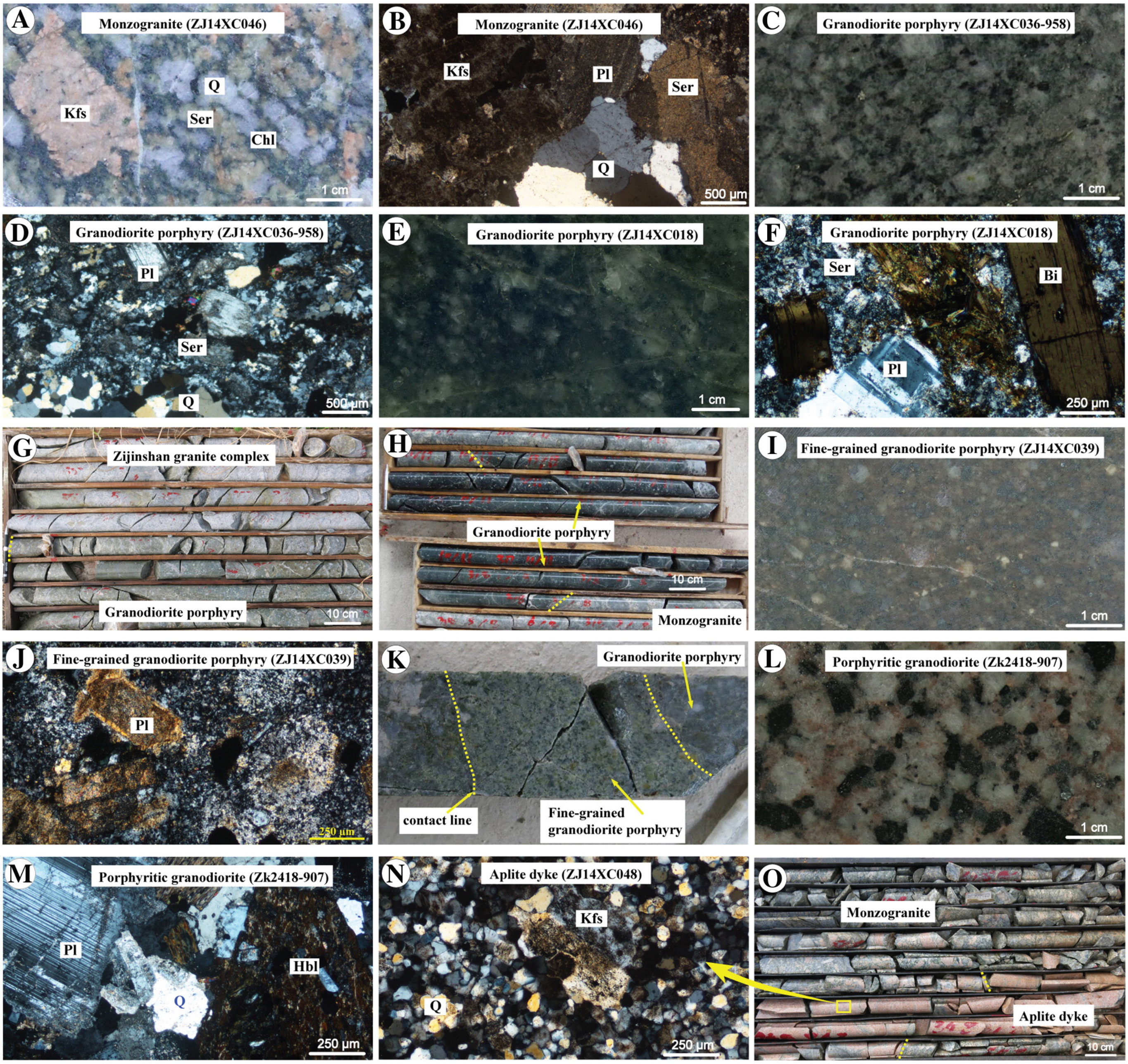

Fig. 3. Photographs of hand specimens and photomicrographs of the igneous rocks and their contact relationships in the Zijinshan Orefield. (A, B) Monzogranite. (C–F) Granodiorite porphyry. (G) Contact between the granodiorite porphyry and the Zijinshan granite complex (Drill-hole ZK327, 821 m deep). (H) Granodiorite porphyry intruded monzogranite (Drill-hole ZK729, 825 m deep). (I, J) Fine-grained granodiorite porphyry. (K) Fine-grained granodiorite porphyry intruded granodiorite porphyry (Drill-hole ZK327, 859 m deep). (L, M) Porphyritic granodiorite. (N) Aplite dyke (cross polarized light). (O) Aplite dyke intruded monzogranite (Drill-hole ZK325, 826 m deep). Abbreviations: Bi–Biotite; Chl–Chlorite; Hbl–Hornblende; Kfs–K-feldspar; Pl-Plagioclase; Q–Quartz; Ser–Sericite.

3. The Xinan granitoids

Granitoids at Xinan were emplaced in the Middle to Late Jurassic and the late Early Cretaceous to earliest Late Cretaceous (Fig. 2). The Zijinshan granite complex including three units as mentioned above (i.e., Jingmei medium-coarse grained granite, Wulongsi medium-fine grained granite and Jinlongqiao fine-grained granite) are widely distributed at shallow levels (above 500 m deep). The monzogranite (Fig. 3A, B) mainly occurs below 500 m deep and locally intruded the Zijinshan granite complex, although the intrusive relationships are subtle due to the intense and pervasive phyllic alteration. The granodiorite porphyry (Fig. 3C–F) occurs as apophyses, intruding along the contact between the Zijinshan granite complex and monzogranite (Fig. 3G, H). The fine-grained granodiorite porphyry (Fig. 3I, J) intruded the granodiorite porphyry (Fig. 3K). The porphyritic granodiorite (Fig. 3L, M) only occurs at depths (intercepted by the Drill Hole Zk2418 at below 400 m deep) and intruded the Zijinshan granite complex. The aplite dykes (Fig. 3N) intruded the monzogranite at depths (intercepted by the Drill Hole Zk327 at 1262 m deep) (Fig. 3O).

4. Analytical methods

In this study, thin sections for 106 samples from the Xinan Cu–Mo deposit were studied under the microscope. Seventeen representative samples (with minimal alteration, cracks and inclusions) were selected for whole-rock geochemical analyses. Six samples were chosen for zircon U–Pb dating and five for in-situ Hf isotope analyses. Photographs of these rocks are shown in Fig. 3 and their characteristics are listed in Table 1.

4.1. Whole rock geochemical analysis

Major and trace elements geochemical analyses were undertaken at the ALS Chemex (Guangzhou) Co. Ltd. Major oxide concentrations were measured by X-ray fluorescence spectrometer on fused glass beads (<200 mesh) using a PANalytical Axios. Fused glass disks with lithium borate were used and the analytical precisions were better than ±0.01%. Trace element concentrations were determined by Inductively Coupled Plasma Mass Spectrometry (ICP-MS) (PerkinElmer Elan 9000), with analytical precision better than ±5% for trace elements. Detailed analytical method and procedure were given in Zhou et al. (2014).

4.2. Zircon U–Pb dating

Zircons were separated by the standard density and magnetic separation techniques, and then hand-picked under a binocular microscope. Representative zircon grains were mounted in epoxy resin and polished to expose the centers of individual crystals. Zircon morphology and internal structure were imaged by using a JXA-8100 Electron Probe Microanalyzer at the Guangzhou Institute of Geochemistry, Chinese Academy of Sciences (GIGCAS).

LA-ICP-MS zircon U–Pb dating and trace element analyses were synchronously conducted on an Agilent 7500 ICP-MS equipped with a 193 nm laser at the Key Laboratory of Mineralogy and Metallogeny, GIGCAS. Laser ablation was operated at a constant energy of 80 mJ, with a repetition rate of 8 Hz and a spot diameter of 31 μm. Helium was used as carrier gas to provide efficient aerosol deposition (Wang et al., 2014). Data were acquired for 30 s with the laser off, and 40 s with the laser on, giving approximately 100 mass scans. NIST SRM 610 glass was used to optimize the machine, while Temora zircon standard (Black et al., 2003) was used as external standards. Each block of five unknowns was bracketed by analyses of standards. Off-line inspection and integration of background and analyze signals, and time-drift correction and quantitative calibration for trace element analyses and U–Pb dating were performed using in-house software ICPMS Data Cal (Liu et al., 2008; Liu et al., 2010). Concordia diagrams and weighted mean calculations were made using Isoplot/Ex_ver3 (Ludwig, 2003). A more detailed analytical technique was described in Yuan et al. (2004).

4.3. In-situ zircon Hf isotope analysis

The in-situ zircon Hf isotope analyses were conducted at the State Key Laboratory of Isotope Geochemistry, GIG CAS, using a Neptune MC-IC-PMS, equipped with a 193 nm laser. All zircon grains were analyzed using a single-spot ablation mode at a spot size of 44 um. The weighted average ^{176}Hf/^{177}Hf value in the zircon standard Penglai was 0.282880 ± 0.000011 (2σ, $n = 10$), which is in good agreement with the recommended Penglai ^{176}Hf/^{177}Hf value of 0.282888 ± 0.000024 (Wu et al., 2015). Detailed operating conditions for the laser ablation system, the MC–ICP–MS instrument, and the analytical method are given by Tang et al. (2012). The ε_{Hf}(t) values were calculated using the chondrite values recommended by Bouvier et al. (2008). The two-stage model ages (T_{DM2}) were calculated using a mean ^{76}Lu/^{177}Hf value of 0.015 for the average continental crust (Griffin et al., 2002).

5. Results

5.1. Whole-rock major and trace elements

Major and trace element data of the representative igneous rocks, including the monzogranite, granodiorite porphyry, fine-grained granodiorite porphyry, porphyritic granodiorite and aplite dyke from Xinan Cu–Mo deposit are presented in Table 2. (See Table 1.)

Table 1
Petrographic features of the Xinan igneous rocks.

Rock type	Texture / structure	Rock-forming minerals	Accessory minerals
Monzogranite (ZJ14XC046)	Heterogranular texture, massive structure	Plagioclase: 30 vol.% (0.5–4.5 mm, some altered to sericite); K-feldspar: 35 vol.% (1–10 mm, some altered); quartz: 30 vol.% (0.2–2 mm); biotite: ~5 vol.% (0.5–2 mm, altered to chlorite) (Fig. 3A, B).	Apatite, zircon
Granodiorite porphyry (ZJ14XC036–958)	Porphyritic texture, massive structure	Phenocrysts (45 vol.%): Plagioclase: 15 vol.% (0.5–3 mm, some altered to sericite); K-feldspar: 5 vol.% (0.5–1 mm, some replaced by sericite and quartz); quartz: 5 vol.% (0.1–2 mm); hornblende and biotite: ~15 vol.% (0.3–2 mm, altered to chlorite and epidote); groundmass (55% vol.%): fine-grained quartz and feldspars (Fig. 3C, D).	Apatite, zircon, magnetite
Granodiorite porphyry (ZJ14XC018)	Porphyritic texture, massive structure	Phenocrysts (45 vol.%): Plagioclase: 20 vol.% (0.5–3 mm, some altered to sericite); K-feldspar: 2 vol.% (0.5–2 mm, some are replaced by clay minerals); quartz: 8 vol.% (0.4–5 mm); hornblende and biotite: ~12 vol.% (0.5–3 mm, altered to chlorite and epidote); groundmass (55%): fine-grained quartz and feldspars altered to sericite (Fig. 3E, F).	Apatite, zircon, magnetite
Fine-grained granodiorite porphyry (ZJ14XC039)	Porphyritic texture, massive structure	Phenocrysts (40 vol.%): Plagioclase: 20 vol.% (0.25–0.8 mm, some altered to sericite); K-feldspar and quartz: 10 vol.% (0.2–0.8 mm); biotite: ~10 vol.% (0.2–1 mm, altered to chlorite and epidote); groundmass (60%): fine-grained quartz and feldspars altered to sericite (Fig. 3I, J).	Apatite, zircon, magnetite
Porphyritic granodiorite (ZK2418–907)	Porphyaceous texture, massive structure	Plagioclase: 40 vol.% (1–5 mm, some altered to sericite); K-feldspar: 5 vol.% (1–2 mm, some altered); quartz: 25 vol.% (0.2–2 mm); hornblende: 15 vol.% (0.5–5 mm, some altered to chlorite); biotite: ~5 vol.% (0.5–2 mm, altered to chlorite) (Fig. 3L, M)	Apatite, zircon, magnetite
Aplite dyke (ZKXC048)	Aplitic texture, massive structure	K-feldspars: 45 vol.% (0.2–0.8 mm, some altered); quartz: 55 vol.% (0.2–0.5 mm) (Fig. 3N).	Apatite, zircon

Table 2
Major and trace elements compositions for the Xinan igneous rocks.

Samples	Monzogranite				Granodiorite porphyry					Fine-grained granodiorite porphyry			Porphyritic granodiorite		Aplite dyke		
	ZJ14XC 142	ZJ14XC 143	ZJ14XC 044	ZJ14XC 046	ZJ14XC 034	ZJ14XC 038	ZJ14XC 018	ZJ14XC 036–958	ZJ14XC 036–948	ZJ14XC 039	ZJ14XC 074	ZJ14XC 136	ZJ14XC 304	ZJ14XC 221	ZJ14XC 001	ZJ14XC 306	ZJ14XC 192
	986 m of zk1931	1004 m of zk1931	1127 m of zk327	1199 m of zk327	826 m of zk327	1050 m of zk327	892 m of zk729	958 m of zk327	948 m of zk327	1019 m of zk327	847 m of zk1127	782 m of zk1931	599 m of zk3203	826 m of zk2418	95 m of zk1216	613 of zk3203	825 m of zk1216
Major oxides %																	
Al_2O_3	14.49	14.93	14.4	14.8	15.1	17.15	15.95	16	14.85	14.65	14.73	15.1	15.86	16.08	13.4	12.94	12.84
BaO	0.14	0.14	0.07	0.15	0.06	0.04	0.07	0.08	0.1	0.1	0.13	0.11	0.1	0.09	0.08	0.08	0.09
CaO	1.66	3.03	2.20	2.80	3.11	5.37	4.15	4.00	2.84	2.23	2.33	1.38	3.66	4.37	1.24	1.70	1.12
Cr_2O_3	0.01	<0.01	0.01	<0.01	0.01	0.01	0.01	0.01	<0.01	<0.01	0.01	0.01	0.01	0.01	0.01	<0.01	0.01
Fe_2O_3	5.86	5.71	5.10	5.02	5.26	5.29	5.37	5.55	4.36	3.73	4.28	4.59	5.12	5.19	2.16	1.90	2.06
K_2O	6.20	4.70	3.88	4.84	3.63	2.28	2.54	3.21	4.24	6.37	5.80	5.32	4.05	3.47	7.03	6.09	6.78
MgO	1.29	1.27	1.31	1.20	2.58	3.92	2.35	1.82	1.69	1.28	1.36	1.66	2.08	1.86	0.50	0.31	0.35
MnO	0.18	0.18	0.18	0.16	0.13	0.20	0.23	0.17	0.15	0.19	0.29	0.18	0.15	0.18	0.10	0.11	0.09
Na_2O	1.58	2.52	2.46	2.75	2.18	1.74	2.54	2.89	3.14	1.76	1.22	1.82	3.25	3.30	1.16	1.22	2.30
P_2O_5	0.22	0.20	0.21	0.21	0.22	0.29	0.26	0.26	0.23	0.19	0.19	0.19	0.26	0.24	0.07	0.07	0.07
SiO_2	64.92	64.79	67.00	65.10	62.30	57.00	63.50	63.30	64.70	65.20	65.77	67.60	62.85	62.72	72.40	72.59	72.87
SrO	0.02	0.04	0.03	0.04	0.03	0.04	0.04	0.06	0.05	0.04	0.03	0.03	0.07	0.07	0.01	0.02	0.02
TiO_2	0.71	0.66	0.69	0.70	0.49	0.78	0.50	0.46	0.42	0.35	0.33	0.35	0.51	0.55	0.21	0.21	0.20
LOI	2.49	2.24	1.98	1.46	3.51	2.73	2.28	1.92	2.36	1.88	3.25	2.71	1.42	1.42	2.04	2.16	1.07
Total	98.64	99.44	99.52	99.23	98.61	99.17	99.79	99.73	99.13	98.83	99.72	100.19	99.39	99.55	100.41	99.40	99.87
Mg#	39	38	37	36	53	55	50	43	47	39	43	51	49	46	35	28	28
A/CNK	1.53	1.46	1.69	1.42	1.69	1.83	1.73	1.58	1.45	1.41	1.58	1.77	1.45	1.44	1.42	1.44	1.26
Trace elements (ppm)																	
Li	24.60	32.50	18.90	33.70	37.90	74.00	40.40	36.00	40.90	16.90	17.70	26.70	39.90	41.20	14.90	42.10	60.90
Be	3.14	4.14	4.43	3.18	2.39	2.07	3.18	2.82	2.54	3.02	2.81	2.56	1.86	1.86	1.69	1.90	2.30
Sc	8.20	7.40	10.00	8.79	11.60	20.50	11.60	10.10	10.50	9.44	5.40	5.70	9.70	8.50	7.14	2.40	2.70
V	58.00	58.00	54.80	57.90	79.60	174.00	77.60	64.30	58.80	41.30	39.00	44.00	84.00	81.00	13.70	14.00	14.00
Cr	18.00	11.00	37.30	16.30	34.20	56.30	54.90	44.10	60.90	36.10	17.00	15.00	26.00	20.00	20.80	13.00	18.00
Co	7.20	5.20	9.42	8.59	19.20	19.40	10.20	15.00	14.20	3.59	8.00	4.20	11.30	8.90	2.23	1.90	2.00
Ni	5.00	5.00	13.60	14.70	10.30	50.70	11.00	11.60	60.20	40.90	2.70	2.80	9.00	9.10	5.74	2.30	2.80
Cu	166.00	44.80	44.91	9.00	213.30	145.80	110.70	293.40	324.00	714.60	41.50	188.00	69.20	8.30	4.71	5.90	6.30
Zn	96.00	69.00	97.20	138.00	58.60	79.50	88.00	108.00	77.40	97.20	147.00	79.00	49.00	48.00	61.00	48.00	28.00
Ga	1.22	2.20	19.70	18.40	16.10	18.70	17.50	17.60	14.70	16.40	1.68	1.05	2.55	3.09	13.70	1.31	0.83
As	3.90	1.20	3.18	2.35	2.39	2.21	3.07	2.00	1.62	2.15	1.90	2.20	2.80	1.40	1.74	1.00	1.90
Rb	261	156	188	170	179	158	117	144	174	255	257	244	152	121	295	284	306

(continued on next page)

Table 2
Major and trace elements compositions for the Xinan igneous rocks.

	Monzogranite				**Granodiorite porphyry**					**Fine-grained granodiorite porphyry**			**Porphyritic granodiorite**		**Aplite dyke**		
	ZJ14XC 142	**ZJ14XC 143**	**ZJ14XC 044**	**ZJ14XC 046**	**ZJ14XC 034**	**ZJ14XC 038**	**ZJ14XC 018**	**ZJ14XC 036–958**	**ZJ14XC 036–948**	**ZJ14XC 039**	**ZJ14XC 074**	**ZJ14XC 136**	**ZJ14XC 304**	**ZJ14XC 221**	**ZJ14XC 001**	**ZJ14XC 306**	**ZJ14XC 192**
Samples	986 m of zk1931	1004 m of zk1931	1127 m of zk327	1199 m of zk327	826 m of zk327	1050 m of zk327	892 m of zk729	958 m of zk327	948 m of zk327	1019 m of zk327	847 m of zk1127	782 m of zk1931	599 m of zk3203	826 m of zk2418	95 m of zk1216	613 of zk3203	825 m of zk1216
Sr	146	284	251	340	207	371	377	520	390	338	216	191	618	541	100	87	150
Y	23.30	27.90	25.60	27.30	18.10	21.00	19.80	14.70	18.00	18.60	15.20	15.00	16.20	14.60	14.60	13.60	15.20
Zr	238.00	219.00	164.00	146.00	101.00	117.00	120.00	121.00	92.60	105.00	119.00	133.00	158.00	107.00	130.00	124.00	127.00
Nb	18.50	22.90	22.10	23.60	16.20	11.50	16.10	15.30	15.40	16.20	11.40	17.40	15.00	17.10	17.50	18.60	19.30
Cs	13.00	7.37	9.89	4.21	11.10	8.56	6.64	2.83	4.08	5.20	5.06	10.10	6.24	5.14	3.39	14.55	2.45
Ba	1140	1200	599	1370	473	371	562	719	840	895	1000	960	770	690	631	610	730
K	51,800	39,600	32,196	38,751	30,121	18,919	21,077	26,636	35,183	52,857	47,800	46,500	33,000	28,300	58,334	51,700	56,700
La	79.20	59.40	69.00	70.20	22.50	20.80	30.30	24.70	23.50	28.20	29.10	25.60	31.40	21.20	45.30	33.20	49.10
Ce	152.50	122.00	128.00	133.00	38.80	39.50	52.60	42.90	40.40	48.90	56.60	50.40	60.50	44.50	83.20	64.30	92.60
Pr	14.95	13.40	13.30	13.80	4.78	5.28	6.38	5.27	4.94	5.91	5.99	5.07	7.16	5.63	8.36	6.55	8.85
Nd	50.40	50.20	45.50	47.90	17.20	20.80	23.20	19.90	17.90	20.80	22.10	18.30	25.30	20.90	27.10	22.00	29.70
Sm	8.03	8.73	7.71	8.34	3.31	4.38	4.36	3.75	3.47	3.87	4.43	3.08	4.61	4.00	4.17	3.44	4.42
Eu	1.47	1.59	1.30	1.54	0.85	1.28	1.12	1.12	0.93	0.90	0.97	0.82	1.09	1.03	0.75	0.62	0.83
Gd	5.75	7.15	6.22	6.71	3.17	4.00	3.71	3.22	3.12	3.34	3.55	2.80	3.50	3.23	3.22	2.52	3.20
Tb	0.89	1.07	0.87	0.95	0.47	0.60	0.53	0.44	0.46	0.50	0.57	0.42	0.53	0.50	0.43	0.43	0.50
Dy	4.88	5.89	4.48	4.87	2.77	3.50	3.09	2.39	2.74	2.89	3.24	2.43	2.84	2.83	2.28	2.43	2.59
Ho	0.96	1.14	0.90	0.98	0.61	0.75	0.66	0.50	0.61	0.62	0.64	0.50	0.65	0.54	0.48	0.51	0.55
Er	2.45	2.74	2.32	2.46	1.74	2.04	1.85	1.38	1.68	1.81	1.85	1.56	1.79	1.47	1.29	1.45	1.47
Tm	0.32	0.43	0.31	0.33	0.26	0.31	0.28	0.20	0.25	0.27	0.30	0.29	0.26	0.26	0.20	0.22	0.24
Yb	2.35	2.55	1.95	2.07	1.88	2.03	1.98	1.44	1.78	1.89	2.06	1.75	1.95	1.69	1.35	1.63	1.57
Lu	0.35	0.38	0.28	0.30	0.30	0.31	0.31	0.24	0.28	0.30	0.32	0.31	0.28	0.27	0.21	0.24	0.25
Hf	0.70	0.70	4.19	3.82	2.95	3.22	3.25	3.33	2.63	3.00	2.00	2.00	0.80	0.90	3.78	2.40	2.40
Ta	1.70	1.90	1.81	1.70	2.01	1.10	1.83	1.75	1.79	1.74	1.70	1.70	1.50	1.60	1.53	1.50	1.50
Tl	1.99	1.10	1.11	0.87	1.15	1.02	0.82	1.10	1.18	2.14	2.77	2.27	1.06	0.80	1.98	2.24	2.39
Pb	46.50	26.30	23.69	30.48	11.10	8.82	9.13	27.26	26.34	24.38	134.00	24.10	53.20	18.90	23.12	20.90	15.10
Th	29.90	25.00	23.60	22.80	13.20	9.56	14.50	11.60	13.30	16.40	15.85	17.40	22.80	18.40	27.30	26.60	30.30
U	5.36	5.63	3.77	3.45	6.24	3.74	5.66	4.65	5.03	6.89	5.78	6.26	7.83	6.11	4.45	3.53	5.27
P	940	910	917	655	961	1266	1135	1135	1004	830	820	860	1140	1050	306	290	290
Ti	3860	3980	4137	2458	2938	4676	2997	2758	2518	2098	1510	2130	3030	3150	1259	1260	1220
Ge	0.23	0.19	1.19	1.20	1.26	1.50	1.37	1.48	1.26	1.50	0.14	0.13	0.15	0.13	0.78	0.15	0.16
Sn	3.90	3.50	3.64	5.85	1.69	3.16	2.49	6.12	2.32	3.21	1.60	3.30	1.50	1.80	1.74	1.50	2.10
Sr/Y	6.24	10.18	9.80	12.45	11.44	17.67	19.04	35.37	21.67	18.17	14.21	12.73	38.15	37.05	6.85	6.37	9.87
Nb/Ta	10.88	12.05	12.24	13.87	8.05	10.42	8.81	8.75	8.58	9.33	6.71	10.24	10.00	10.69	11.44	12.40	12.87
$(La/Yb)_N$	24.17	16.71	25.38	24.33	8.58	7.35	10.98	12.30	9.47	10.70	10.13	10.49	11.55	9.00	24.07	14.61	22.43
$(Gd/Yb)_N$	2.02	2.32	2.64	2.68	1.39	1.63	1.55	1.85	1.45	1.46	1.43	1.32	1.48	1.58	1.97	1.28	1.69
$\sum$ REE	324.500	276.670	282.140	293.447	98.641	105.591	130.376	107.453	102.059	120.199	131.720	113.330	141.860	108.050	178.334	139.540	195.870
LREE/HREE	17.08	11.96	15.28	14.72	7.81	6.80	9.50	9.95	8.34	9.35	9.51	10.27	11.02	9.01	17.86	13.80	17.89
Eu/Eu*	0.63	0.60	0.56	0.61	0.79	0.92	0.83	0.96	0.84	0.75	0.72	0.84	0.80	0.85	0.60	0.62	0.64

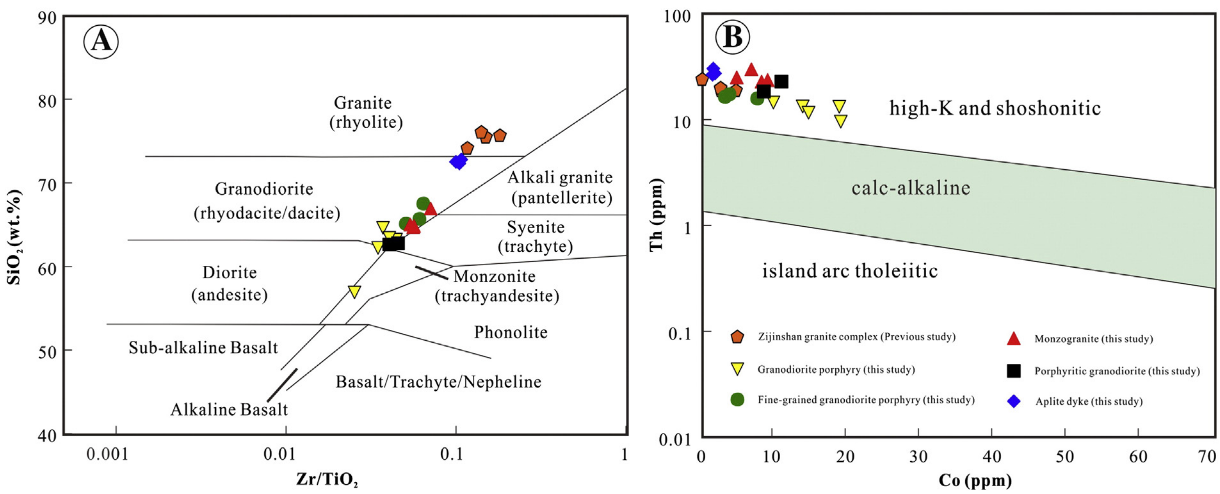

Fig. 4. Discrimination diagrams for the igneous rocks in the Zijinshan Orefield. A: Zr/TiO_2 vs. SiO_2 (after Winchester and Floyd, 1977). B: Co vs. Th diagram (after Hastie et al., 2007). Data of the Zijinshan complex granite are from Zhang et al. (2001).

5.1.1. Major elements

The Xinan granitoids are generally high in SiO_2 (57.00–72.87 wt.%) and Al_2O_3 (12.84–17.15 wt.%), low in TiO_2 (0.20–0.78 wt.%), Fe_2O_3 (1.9–7.62 wt.%), MgO (0.31–3.92 wt.%) and P_2O_5 (0.07–0.29 wt.%). The $Mg^{\#}$ values of the Xinan granodiorite porphyry, fine-grained granodiorite porphyry and porphyritic granodiorite (39–55, mostly 43–55) are higher than the Zijinshan granite complex, monzogranite and aplite dyke (28–49, mostly 28–39).

From the SiO_2 vs. Zr/TiO_2 (Fig. 4A) (Winchester and Floyd, 1977) and Th vs. Co diagrams (Fig. 4B) (Hastie et al., 2007), the Zijinshan granitoids are mainly classified as high-K calc-alkaline / shoshonitic granodiorite-granite.

5.1.2. Trace elements

In the chondrite-normalized REE diagram, the Xinan monzogranite (Fig. 5A) and aplite dyke (Fig. 5G) are LREE-enriched and HREE-depleted ($\sum$REE = 140–325, LREE/HREE = 11.96–17.89), contain moderately high $(La/Yb)_N$ (14.61–25.38) (Table 2) and negative Eu anomalies ($Eu/Eu^* = 0.56$–0.64, Table 2). The Xinan granodiorite porphyry, fine-grained granodiorite porphyry and porphyritic granodiorite (Fig. 5C, E) are also LREE-enriched and HREE-depleted ($\sum$REE = 99–142, LREE/HREE = 6.80–11.02), but contain low $(La/Yb)_N$ (7.35–12.30) (Table 2) and no obvious Eu anomalies ($Eu/Eu^* = 0.72$–0.96, Table 2). In the primitive mantle-normalized multi-element diagrams (Fig. 5B, D, F, H), all the Xinan granitoids are enriched in large-ion lithophile elements (LILE, e.g. Rb, Ba, U, K, Pb and Sr), and depleted in high-field strength elements (HFSE, e.g. Nb, Ta, Hf, Ti). The Zijinshan complex granite is LREE-enriched and HREE-depleted (Fig. 5), shows moderately high $(La/Yb)_N$ (2.85–18.54) and strong negative Eu anomalies ($Eu/Eu^* = 0.29$–0.60).

5.2. Zircon U–Pb ages

Representative zircon CL images and analytical spots for the six dated samples are shown in Fig. 6, and the detailed U–Pb analytical data are listed in Table 3 and illustrated in Fig. 7.

5.2.1. Monzogranite

Zircons from the Zijinshan monzogranite (ZJ14XC046) are generally euhedral and prismatic. They have Th/U ratios of 0.27 to 0.74 and show clear igneous oscillatory zoning, indicating a magmatic origin (Fig. 6). Excluding seven discordant analyses, twenty-two analyses yielded concordant $^{206}Pb/^{238}U$ ages ranging from 163 to 154 Ma, and a weighted mean age of 156.9 ± 1.0 Ma (MSWD = 0.8, Fig. 7A).

5.2.2. Granodiorite porphyry

Zircons from the two granodiorite porphyry (ZJ14XC036–958 and ZJ14XC018) are subhedral to euhedral. They have Th/U ratios of 0.23 to 0.44 and clear igneous oscillatory zoning, suggesting a magmatic origin (Fig. 6). Twenty-one zircons from the sample ZJ14XC036–958 yielded concordant $^{206}Pb/^{238}U$ ages ranging from 113 to 106 Ma, and a weighted mean age of 108.9 ± 1.0 Ma (MSWD = 1.8, Fig. 7B). Twenty-two zircons from the sample ZJ14XC018 yielded concordant $^{206}Pb/^{238}U$ ages ranging from 114 to 105 Ma, and a weighted mean age of 109.2 ± 0.9 Ma (MSWD = 1.7, Fig. 7C).

5.2.3. Fine-grained granodiorite porphyry

The fine-grained granodiorite porphyry (ZJ14XC039) contains subhedral to euhedral zircons. They have Th/U ratios of 0.27 to 0.47 and oscillatory zoning, suggestive of a magmatic origin (Fig. 6). Excluding four discordant analyses, twenty-six zircons yielded concordant $^{206}Pb/^{238}U$ ages ranging from 110 to 105 Ma, and a weighted mean age of 107.0 ± 0.8 Ma (MSWD = 1.3, Fig. 7D).

5.2.4. Porphyritic granodiorite

Porphyritic granodiorite (Zk2418–907) contains subhedral to euhedral zircons. They have Th/U ratios of 0.38 to 0.67 and oscillatory zoning, suggestive of a magmatic origin (Fig. 6). Excluding five discordant zircons, twenty zircons yielded concordant $^{206}Pb/^{238}U$ ages ranging from 106 to 99 Ma and a weighted mean age of 102.7 ± 0.7 Ma (MSWD = 1.0, Fig. 7E).

5.2.5. Aplite dyke

Zircon grains from the aplite dyke (ZJ14XC048) are subhedral to euhedral (Fig. 6). Seventeen out of 25 zircons plot on a concordia line. Seven zircons (Th/U ratios: 0.39–0.54) yielded concordant $^{206}Pb/^{238}U$ ages ranging from 107 to 98.5 Ma, with a weighted mean age of 102.3 ± 2.6 Ma (MSWD = 3.0, Fig. 7H). For the older (probably inherited) zircons, seven zircons (Th/U ratios: 0.36–0.88) yielded concordant $^{206}Pb/^{238}U$ ages ranging from 145 to 138 Ma and a weighted mean age of 141.1 ± 2.5 Ma (MSWD = 1.8, Fig. 7G). Two zircons yielded $^{206}Pb/^{238}U$ ages of 160.0 ± 2.7 Ma and 159.0 ± 2.7 Ma. One zircon (Th/U ratio: 0.35) yielded $^{206}Pb/^{238}U$ ages of 840.0 ± 22.8 Ma.

5.3. Zircon Ce4+/Ce3+ ratios

Zircon Ce^{4+}/Ce^{3+} values, a measure of the oxidation state of the magma (Ballard et al., 2002; Liang et al., 2006; Wu et al., 2015), of the Xinan samples were calculated using the same data collected during

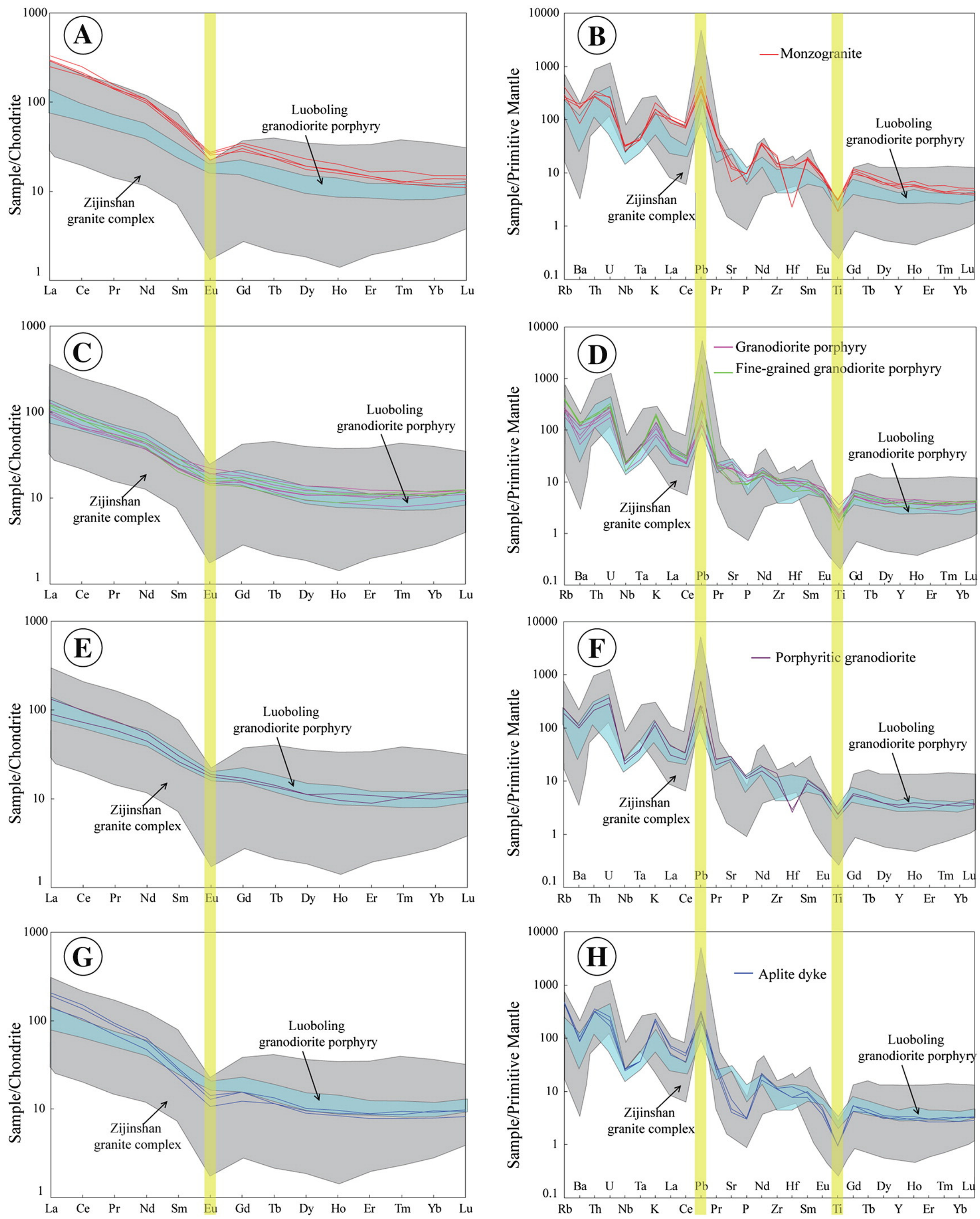

Fig. 5. Chondrite-normalized REE diagram and primitive mantle-normalized multi-element spider diagram for the igneous rocks in the Zijinshan Orefield. Chondrite-normalization and primitive mantle-normalization values are from Sun. and McDonough (1989). The gray field represents the Zijinshan granite complex data (Jiang et al., 2013; Huang, 2014), and the blue field represents the Luoboling granodiorite porphyry data (Huang, 2014). (For interpretation of the references to colour in this figure legend, the reader is referred to the web version of this article.)

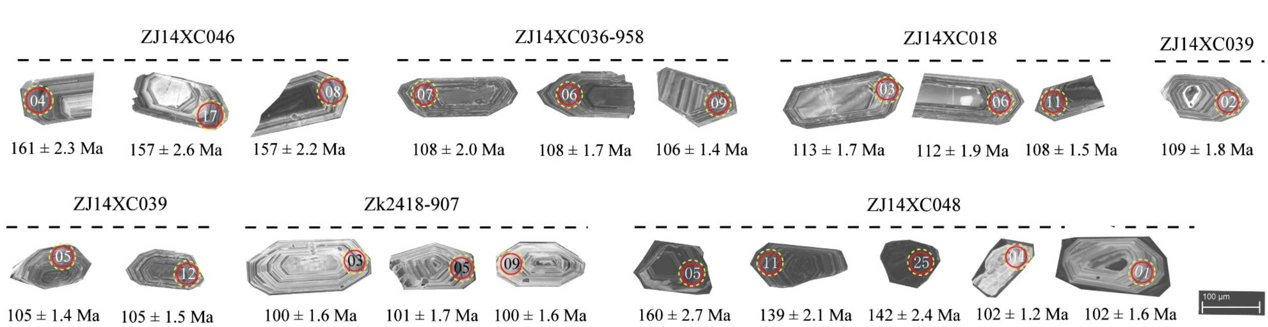

Fig. 6. Representative zircon CL images and analyzed spots with U–Pb ages.

Table 3
LA-ICP-MS zircon U–Pb data and Ce^{4+}/Ce^{3+} values for the Xinan igneous rocks.

Analysis	Content (ppm)				Isotopic ratios						Isotopic ages (Ma)						
	Pb	Th	U	Th/U	$^{207}Pb/^{206}Pb$	± 1σ	$^{207}Pb/^{235}U$	± 1σ	$^{206}Pb/^{238}U$	± 1σ	$^{207}Pb/^{206}Pb$	± 1σ	$^{207}Pb/^{235}U$	± 1σ	$^{206}Pb/^{238}U$	± 1σ	Ce^{4+}/Ce^{3+}
Monzogranite																	
zj14xc046–02	43	524	1516	0.35	0.0508	0.0014	0.1779	0.0054	0.0254	0.0004	232	64.8	166	4.6	162	2.7	393.36
zj14xc046–03	119	1134	4097	0.28	0.0504	0.0012	0.1778	0.0048	0.0255	0.0004	213	89.8	166	4.1	163	2.5	230.91
zj14xc046–04	38	505	1253	0.40	0.0504	0.0013	0.1759	0.0048	0.0252	0.0004	213	59.2	164	4.1	161	2.3	145.64
zj14xc046–06	45	614	1521	0.40	0.0506	0.0016	0.1731	0.0060	0.0247	0.0004	220	76.8	162	5.2	157	2.8	117.04
zj14xc046–07	15	262	503	0.52	0.0517	0.0018	0.1718	0.0058	0.0242	0.0004	333	81.5	161	5.0	154	2.6	168.21
zj14xc046–08	24	314	820	0.38	0.0506	0.0017	0.1716	0.0054	0.0246	0.0003	220	75.9	161	4.7	157	2.2	148.06
zj14xc046–09	61	662	2115	0.31	0.0500	0.0012	0.1686	0.0040	0.0244	0.0003	198	57.4	158	3.5	155	1.8	347.30
zj14xc046–10	27	524	852	0.62	0.0495	0.0015	0.1683	0.0051	0.0246	0.0004	172	70.4	158	4.5	157	2.3	210.62
zj14xc046–11	44	566	1535	0.37	0.0497	0.0014	0.1693	0.0054	0.0246	0.0004	189	73.1	159	4.7	157	2.7	373.09
zj14xc046–12	5	86	184	0.47	0.0502	0.0030	0.1685	0.0096	0.0245	0.0005	211	144	158	8.4	156	2.8	178.75
zj14xc046–13	35	385	1215	0.32	0.0515	0.0019	0.1763	0.0056	0.0247	0.0004	265	78.7	165	4.8	157	2.6	156.65
zj14xc046–16	75	1572	2451	0.64	0.0491	0.0019	0.1665	0.0058	0.0243	0.0004	154	90.7	156	5.1	155	2.6	202.85
zj14xc046–17	30	386	1003	0.39	0.0495	0.0020	0.1698	0.0063	0.0247	0.0004	169	94.4	159	5.5	157	2.6	247.24
zj14xc046–18	36	489	1196	0.41	0.0507	0.0017	0.1737	0.0055	0.0246	0.0004	228	75.9	163	4.8	157	2.7	348.37
zj14xc046–19	27	295	913	0.32	0.0492	0.0017	0.1681	0.0057	0.0247	0.0004	154	81.5	158	4.9	157	2.7	457.06
zj14xc046–20	33	363	1130	0.32	0.0520	0.0017	0.1781	0.0065	0.0247	0.0004	287	75.9	166	5.6	157	2.7	27.40
zj14xc046–21	62	1048	1976	0.53	0.0479	0.0015	0.1647	0.0054	0.0248	0.0004	95	74.1	155	4.7	158	2.5	111.00
zj14xc046–22	30	423	1019	0.41	0.0461	0.0015	0.1561	0.0051	0.0244	0.0004	400.1	error	147	4.5	155	2.2	282.01
zj14xc046–25	30	673	909	0.74	0.0475	0.0019	0.1610	0.0062	0.0242	0.0004	72.3	92.585	152	5.4	154	2.6	159.22
zj14xc046–26	53	591	1811	0.33	0.0505	0.0019	0.1725	0.0063	0.0244	0.0004	217	87.0	162	5.5	155	2.6	128.69
zj14xc046–27	69	782	2338	0.33	0.0492	0.0015	0.1670	0.0052	0.0243	0.0004	154	74.1	157	4.5	155	2.4	440.40
zj14xc046–28	26	239	896	0.27	0.0521	0.0017	0.1787	0.0062	0.0246	0.0005	300	74.1	167	5.4	157	2.9	207.03
Granodiorite porphyry																	
zj14xc036–958-21	31	479	1486	0.32	0.0504	0.0016	0.1234	0.0042	0.0177	0.0003	213	44	118	4	113	2.0	1075.67
zj14xc036–958-17	26	481	1197	0.40	0.0498	0.0016	0.1214	0.0043	0.0175	0.0003	187	76	116	4	112	1.7	1098.25
zj14xc036–958-23	35	527	1732	0.30	0.0506	0.0016	0.1223	0.0040	0.0175	0.0003	233	72	117	4	112	2.0	1334.98
zj14xc036–958-27	29	540	1406	0.38	0.0492	0.0016	0.1191	0.0041	0.0175	0.0003	167	76	114	4	112	1.9	1490.77
zj14xc036–958-18	39	554	1898	0.29	0.0474	0.0014	0.1144	0.0034	0.0174	0.0003	78	61	110	3	111	1.6	1201.15
zj14xc036–958-20	40	562	2000	0.28	0.0494	0.0015	0.1184	0.0036	0.0174	0.0003	169	70	114	3	111	1.9	1568.37
zj14xc036–958-02	27	389	1326	0.29	0.0505	0.0015	0.1210	0.0038	0.0173	0.0003	217	70	116	3	111	1.7	973.58
zj14xc036–958-29	28	450	1382	0.33	0.0499	0.0016	0.1185	0.0038	0.0173	0.0003	191	69	114	3	110	1.9	1339.26
zj14xc036–958-04	32	602	1563	0.38	0.0492	0.0014	0.1169	0.0035	0.0172	0.0003	167	60	112	3	110	1.6	1045.48
zj14xc036–958-16	40	635	1963	0.32	0.0493	0.0016	0.1170	0.0039	0.0171	0.0002	161	78	112	4	109	1.5	1294.73
zj14xc036–958-08	42	566	2059	0.27	0.0463	0.0012	0.1085	0.0028	0.0170	0.0003	13	65	105	3	109	1.6	1367.01
zj14xc036–958-26	34	699	1692	0.41	0.0493	0.0017	0.1157	0.0040	0.0170	0.0003	161	80	111	4	109	1.8	996.20
zj14xc036–958-07	32	469	1559	0.30	0.0493	0.0016	0.1150	0.0041	0.0169	0.0003	165	74	111	4	108	2.0	201.89
zj14xc036–958-30	32	383	1668	0.23	0.0499	0.0014	0.1167	0.0036	0.0169	0.0003	191	67	112	3	108	1.6	1172.12
zj14xc036–958-13	36	552	1700	0.33	0.0469	0.0013	0.1094	0.0031	0.0169	0.0002	56	67	105	3	108	1.5	1322.41
zj14xc036–958-06	35	514	1703	0.30	0.0495	0.0015	0.1155	0.0040	0.0169	0.0003	169	72	111	4	108	1.7	541.85
zj14xc036–958-10	47	583	2235	0.26	0.0488	0.0011	0.1129	0.0031	0.0168	0.0003	200	54	109	3	107	1.7	1683.67
zj14xc036–958-15	45	935	2145	0.44	0.0484	0.0015	0.1120	0.0036	0.0168	0.0003	117	74	108	3	107	1.7	702.21
zj14xc036–958-09	29	472	1413	0.33	0.0470	0.0013	0.1074	0.0029	0.0166	0.0002	56	67	104	3	106	1.4	1074.52
zj14xc036–958-12	37	761	1774	0.43	0.0489	0.0014	0.1116	0.0032	0.0165	0.0002	143	67	107	3	106	1.3	658.21
zj14xc036–958-11	38	749	1852	0.40	0.0461	0.0013	0.1047	0.0030	0.0165	0.0003	400	error	101	3	106	1.6	1176.84
Granodiorite porphyry																	
ZJ14XC018–01	32	422	1607	0.26	0.0015	0.1154	0.0039	0.0172	0.0003	0.4405	122	74	111	4	110	1.6	1605.53
ZJ14XC018–03	20	297	962	0.31	0.0018	0.1122	0.0039	0.0176	0.0003	0.4513	9	89	108	4	113	1.7	1364.78
ZJ14XC018–04	35	579	1704	0.34	0.0013	0.1114	0.0032	0.0172	0.0002	0.4743	32	67	107	3	110	1.5	1175.60
ZJ14XC018–05	24	362	1165	0.31	0.0014	0.1092	0.0034	0.0171	0.0003	0.5207	9	70	105	3	109	1.8	858.72
ZJ14XC018–06	25	348	1203	0.29	0.0016	0.1167	0.0040	0.0175	0.0003	0.4892	117	78	112	4	112	1.9	1660.93
ZJ14XC018–07	30	514	1457	0.35	0.0014	0.1067	0.0030	0.0171	0.0003	0.5932	error	error	103	3	110	1.8	1111.62

Table 3
LA-ICP-MS zircon U–Pb data and Ce^{4+}/Ce^{3+} values for the Xinan igneous rocks.

Analysis	Content (ppm)			Th/U	Isotopic ratios						Isotopic ages (Ma)						Ce^{4+}/Ce^{3+}
	Pb	Th	U		$^{207}Pb/^{206}Pb$	± 1σ	$^{207}Pb/^{235}U$	± 1σ	$^{206}Pb/^{238}U$	± 1σ	$^{207}Pb/^{206}Pb$	± 1σ	$^{207}Pb/^{235}U$	± 1σ	$^{206}Pb/^{238}U$	± 1σ	
ZJ14XC018–08	21	245	1086	0.23	0.0016	0.1109	0.0037	0.0169	0.0002	0.4399	76	74	107	3	108	1.6	915.96
ZJ14XC018–09	26	394	1288	0.31	0.0014	0.1101	0.0034	0.0169	0.0002	0.4468	50	74	106	3	108	1.5	661.35
ZJ14XC018–10	30	575	1348	0.43	0.0016	0.1167	0.0040	0.0177	0.0003	0.5116	95	81	112	4	113	2.0	586.82
ZJ14XC018–11	27	469	1324	0.35	0.0015	0.1113	0.0036	0.0169	0.0002	0.4250	80	error	107	3	108	1.5	883.99
ZJ14XC018–12	60	777	2973	0.26	0.0013	0.1133	0.0033	0.0171	0.0003	0.5303	100	58	109	3	109	1.7	433.61
ZJ14XC018–14	33	512	1583	0.32	0.0014	0.1148	0.0037	0.0171	0.0002	0.4112	120	66	110	3	109	1.4	1111.37
ZJ14XC018–15	35	628	1698	0.37	0.0016	0.1142	0.0037	0.0169	0.0002	0.4504	143	76	110	3	108	1.6	479.29
ZJ14XC018–16	30	431	1484	0.29	0.0015	0.1071	0.0036	0.0169	0.0002	0.4375	error	error	103	3	108	1.6	1181.28
ZJ14XC018–17	19	476	849	0.56	0.0016	0.1102	0.0041	0.0175	0.0003	0.3946	error	error	106	4	112	1.6	1298.56
ZJ14XC018–18	40	612	1949	0.31	0.0013	0.1148	0.0033	0.0169	0.0002	0.4518	154	63	110	3	108	1.4	531.38
ZJ14XC018–19	30	407	1536	0.26	0.0013	0.1109	0.0031	0.0168	0.0002	0.4578	100	60	107	3	107	1.4	1706.02
ZJ14XC018–20	40	797	1897	0.42	0.0013	0.1161	0.0033	0.0171	0.0002	0.4817	143	61	112	3	110	1.5	843.74
ZJ14XC018–21	23	641	995	0.64	0.0017	0.1161	0.0040	0.0178	0.0002	0.3992	61	81	112	4	114	1.6	616.67
ZJ14XC018–22	31	575	1496	0.38	0.0017	0.1152	0.0035	0.0168	0.0003	0.4933	187	78	111	3	107	1.6	798.96
ZJ14XC018–23	33	464	1614	0.29	0.0015	0.1116	0.0037	0.0171	0.0003	0.4891	54	74	107	3	109	1.8	1687.11
ZJ14XC018–24	29	408	1475	0.28	0.0016	0.1076	0.0036	0.0164	0.0002	0.4191	58	143	104	3	105	1.5	1358.54
Fine-grained granodiorite porphyry																	
zj14xc039–01	23	337	1185	0.28	0.0015	0.1079	0.0032	0.0170	0.0003	0.5666	error	error	104	3	109	1.8	1159.97
zj14xc039–02	22	383	1058	0.36	0.0017	0.1171	0.0043	0.0171	0.0003	0.4263	167	81	112	4	109	1.7	259.96
zj14xc039–03	21	440	1003	0.44	0.0025	0.1214	0.0055	0.0171	0.0003	0.3692	265	113	116	5	109	1.8	638.13
zj14xc039–04	28	465	1353	0.34	0.0014	0.1158	0.0033	0.0170	0.0003	0.5155	167	60	111	3	109	1.6	519.26
zj14xc039–05	21	289	1072	0.27	0.0017	0.1185	0.0040	0.0164	0.0002	0.4070	295	76	114	4	105	1.4	1165.66
zj14xc039–06	17	239	876	0.27	0.0019	0.1070	0.0044	0.0167	0.0003	0.3764	32	93	103	4	107	1.6	850.02
zj14xc039–09	20	308	976	0.32	0.0017	0.1202	0.0040	0.0173	0.0004	0.6675	228	80	115	4	110	2.4	765.52
zj14xc039–12	17	263	871	0.30	0.0015	0.1149	0.0032	0.0163	0.0002	0.5384	261	69	110	3	105	1.5	710.89
zj14xc039–13	26	454	1292	0.35	0.0013	0.1139	0.0030	0.0169	0.0002	0.5548	165	66	109	3	108	1.5	1123.47
zj14xc039–14	21	329	1004	0.33	0.0016	0.1099	0.0038	0.0172	0.0003	0.4551	50	81	106	3	110	1.7	1159.49
zj14xc039–15	24	449	1133	0.40	0.0024	0.1269	0.0044	0.0172	0.0003	0.4537	409	96	121	4	110	1.7	627.77
zj14xc039–16	19	347	957	0.36	0.0016	0.1066	0.0036	0.0166	0.0003	0.4525	61	78	103	3	106	1.6	690.66
zj14xc039–17	20	390	964	0.40	0.0016	0.1099	0.0034	0.0164	0.0002	0.3977	143	78	106	3	105	1.3	929.59
zj14xc039–18	25	565	1241	0.46	0.0019	0.1174	0.0042	0.0164	0.0002	0.3627	287	79	113	4	105	1.4	239.07
zj14xc039–19	17	245	885	0.28	0.0019	0.1139	0.0041	0.0164	0.0002	0.4069	217	87	109	4	105	1.5	1014.50
zj14xc039–20	22	377	1060	0.36	0.0018	0.1102	0.0041	0.0172	0.0003	0.4078	20	89	106	4	110	1.6	1119.28
zj14xc039–21	25	432	1230	0.35	0.0017	0.1129	0.0038	0.0166	0.0003	0.4550	146	83	109	3	106	1.6	751.72
zj14xc039–22	21	345	1065	0.32	0.0017	0.1156	0.0041	0.0167	0.0003	0.5102	176	77	111	4	107	1.9	717.38
zj14xc039–23	42	964	2050	0.47	0.0015	0.1141	0.0037	0.0167	0.0003	0.5775	150	70	110	3	107	2.0	671.64
zj14xc039–24	23	424	1116	0.38	0.0017	0.1088	0.0040	0.0168	0.0003	0.4604	32	85	105	4	107	1.8	831.58
zj14xc039–25	17	276	827	0.33	0.0017	0.1109	0.0040	0.0168	0.0002	0.4053	65	85	107	4	107	1.6	606.85
zj14xc039–26	22	337	1095	0.31	0.0018	0.1097	0.0043	0.0169	0.0003	0.4265	33	83	106	4	108	1.8	777.72
zj14xc039–27	27	489	1312	0.37	0.0018	0.1133	0.0039	0.0166	0.0003	0.5065	161	90	109	4	106	1.8	648.37
zj14xc039–28	23	457	1133	0.40	0.0016	0.1103	0.0035	0.0166	0.0002	0.4572	102	84	106	3	106	1.5	730.96
zj14xc039–29	25	470	1184	0.40	0.0015	0.1157	0.0039	0.0172	0.0003	0.5780	124	69	111	4	110	2.1	733.79
zj14xc039–30	28	476	1371	0.35	0.0013	0.1070	0.0033	0.0165	0.0002	0.4621	28	67	103	3	106	1.5	1181.29
Porphyritic granodioirte																	
zk2418–907-09	12	292	624	0.47	0.0021	0.1043	0.0045	0.0157	0.0002	0.3668	106	100	101	4	100	1.6	630.91
zk2418–907-16	15	350	731	0.48	0.0022	0.1084	0.0051	0.0162	0.0003	0.3921	128	107	105	5	104	1.9	944.26
zk2418–907-19	12	275	606	0.45	0.0019	0.1079	0.0046	0.0162	0.0003	0.4334	102	error	104	4	104	1.9	263.95
zk2418–907-23	18	465	931	0.50	0.0017	0.1062	0.0036	0.0160	0.0002	0.4391	120	81	102	3	102	1.5	372.05
zk2418–907-04	14	313	687	0.46	0.0020	0.1035	0.0043	0.0159	0.0002	0.3752	65	96	100	4	102	1.6	814.18
zk2418–907-05	19	571	930	0.61	0.0017	0.1030	0.0038	0.0158	0.0003	0.4555	61	89	100	4	101	1.7	546.17
zk2418–907-24	14	274	712	0.39	0.0016	0.1077	0.0038	0.0160	0.0002	0.4223	143	76	104	3	102	1.5	847.82
zk2418–907-25	13	246	641	0.38	0.0017	0.1067	0.0034	0.0163	0.0003	0.5510	106	81	103	3	104	1.8	815.46

(continued on next page)

Table 3 (*continued*)

Analysis	Content (ppm)			Th/U	Isotopic ratios						Isotopic ages (Ma)						Ce^{4+}/Ce^{3+}
	Pb	Th	U		$^{207}Pb/^{206}Pb$	± 1σ	$^{207}Pb/^{235}U$	± 1σ	$^{206}Pb/^{238}U$	± 1σ	$^{207}Pb/^{206}Pb$	± 1σ	$^{207}Pb/^{235}U$	± 1σ	$^{206}Pb/^{238}U$	± 1σ	
zk2418–907-02	14	304	722	0.42	0.0019	0.1041	0.0042	0.0161	0.0002	0.3736	39	93	101	4	103	1.5	1004.27
zk2418–907-13	13	278	638	0.44	0.0017	0.1094	0.0036	0.0161	0.0003	0.5614	176	77	105	3	103	1.9	1056.07
zk2418–907-22	14	346	674	0.51	0.0022	0.1129	0.0050	0.0163	0.0003	0.3508	198	102	109	5	105	1.6	404.68
zk2418–907-03	12	315	645	0.49	0.0019	0.1087	0.0042	0.0156	0.0003	0.4266	217	85	105	4	100	1.6	852.63
zk2418–907-06	15	340	784	0.43	0.0020	0.0978	0.0043	0.0155	0.0003	0.3944	error	error	95	4	99	1.7	938.66
zk2418–907-18	20	430	1039	0.41	0.0016	0.1110	0.0033	0.0160	0.0002	0.4535	220	77	107	3	102	1.4	1121.75
zk2418–907-01	10	220	524	0.42	0.0018	0.1028	0.0039	0.0163	0.0003	0.4424	error	error	99	4	105	1.8	1323.87
zk2418–907-14	16	363	774	0.47	0.0017	0.1125	0.0037	0.0160	0.0003	0.4880	243	80	108	3	102	1.7	594.44
zk2418–907-12	14	352	682	0.52	0.0017	0.1133	0.0038	0.0160	0.0003	0.4732	250	78	109	3	102	1.6	420.16
zk2418–907-21	14	308	673	0.46	0.0020	0.1194	0.0044	0.0166	0.0003	0.4922	306	87	115	4	106	1.9	325.34
zk2418–907-11	23	733	1093	0.67	0.0016	0.1149	0.0038	0.0159	0.0003	0.5262	300	72	110	3	102	1.7	513.84
zk2418–907-15	13	289	695	0.42	0.0017	0.1142	0.0039	0.0157	0.0003	0.4698	309	77	110	4	101	1.6	798.31
Aplite dyke																	
ZJ14XC048–23	17	435	807	0.54	0.0515	0.0020	0.1200	0.0051	0.0167	0.0002	265	89	115	5	107	1.6	190.04
ZJ14XC048–10	15	372	762	0.49	0.0453	0.0017	0.1022	0.0041	0.0164	0.0003	error	error	99	4	105	1.7	410.57
ZJ14XC048–14	13	317	651	0.49	0.0519	0.0019	0.1142	0.0041	0.0161	0.0003	280	85	110	4	103	1.7	419.01
ZJ14XC048–04	12	267	596	0.45	0.0511	0.0020	0.1129	0.0048	0.0160	0.0003	256	89	109	4	102	1.8	363.33
ZJ14XC048–01	16	377	819	0.46	0.0482	0.0017	0.1051	0.0037	0.0159	0.0003	109	81	101	3	102	1.6	641.03
ZJ14XC048–17	9	190	481	0.39	0.0521	0.0024	0.1128	0.0050	0.0158	0.0003	300	101	109	5	101	1.7	389.93
ZJ14XC048–15	13	320	692	0.46	0.0476	0.0022	0.1007	0.0048	0.0154	0.0002	80	111	97	4	98	1.4	481.90
Inherited zircon																	
ZJ14XC048–05	161	2476	5362	0.46	0.0491	0.0012	0.1706	0.0047	0.0252	0.0004	150	56	160	4	160	2.7	
ZJ14XC048–18	44	808	1396	0.58	0.0515	0.0014	0.1754	0.0044	0.0249	0.0004	265	63	164	4	159	2.7	
ZJ14XC048–19	74	956	2691	0.36	0.0500	0.0011	0.1566	0.0035	0.0227	0.0003	195	50	148	3	145	1.6	
ZJ14XC048–24	55	1531	1740	0.88	0.0490	0.0015	0.1529	0.0047	0.0225	0.0004	146	70	144	4	144	2.2	
ZJ14XC048–25	160	2190	5878	0.37	0.0512	0.0016	0.1578	0.0051	0.0222	0.0004	256	70	149	4	142	2.4	
ZJ14XC048–22	142	2264	5353	0.42	0.0509	0.0012	0.1556	0.0038	0.0221	0.0003	235	49	147	3	141	1.8	
ZJ14XC048–11	75	1167	2896	0.40	0.0478	0.0013	0.1435	0.0042	0.0218	0.0003	87	58	136	4	139	2.1	
ZJ14XC048–13	18	441	638	0.69	0.0491	0.0017	0.1478	0.0055	0.0218	0.0003	154	77	140	5	139	2.1	
ZJ14XC048–08	138	2163	5169	0.42	0.0481	0.0011	0.1438	0.0037	0.0216	0.0003	106	58	136	3	138	2.1	
ZJ14XC048–12	8	17.2	48.5	0.35	0.0651	0.0039	1.2556	0.0834	0.1392	0.0040	777	122	826	38	840	22.8	

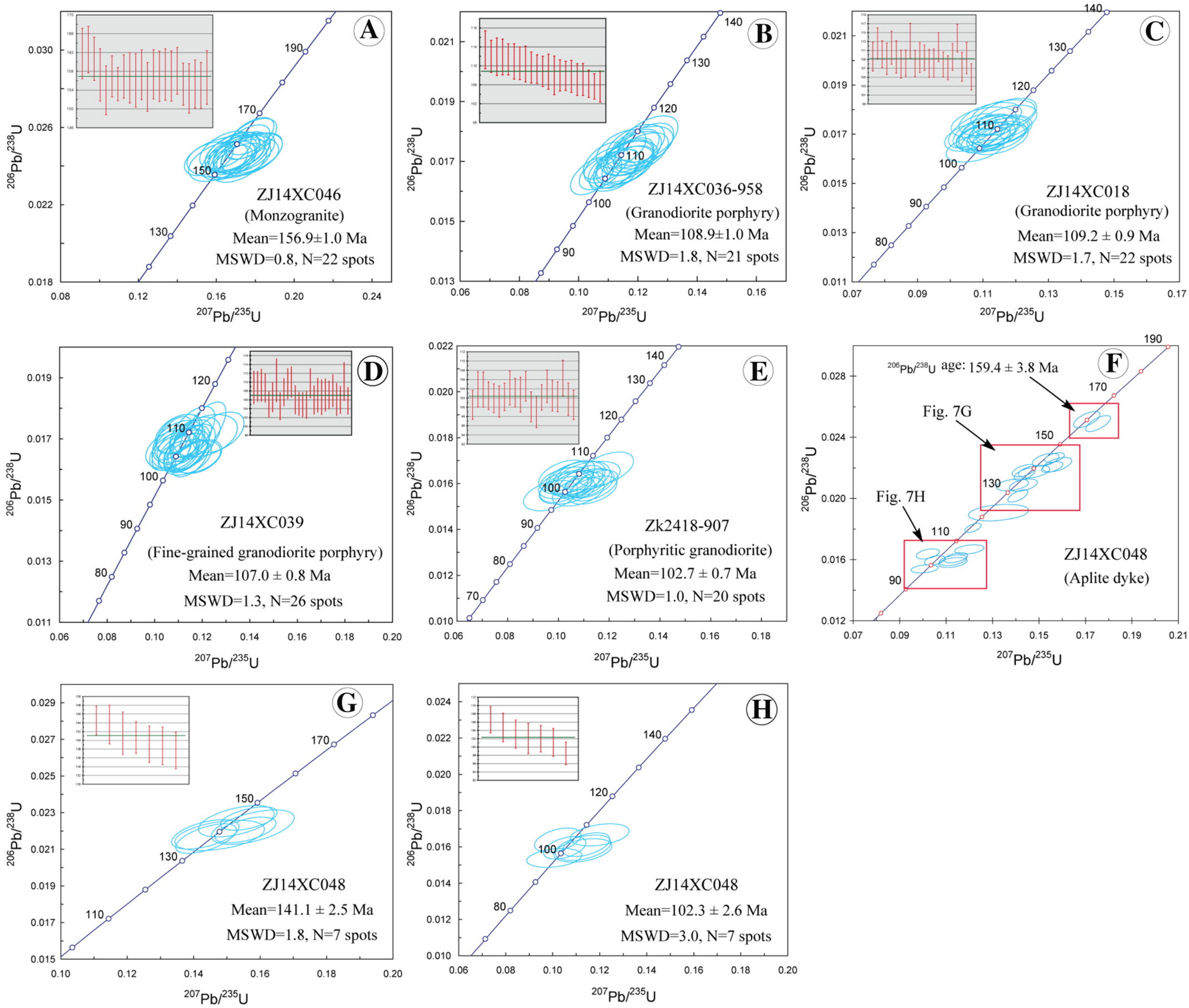

Fig. 7. Zircon U–Pb concordia diagram and weighted mean $^{206}Pb/^{238}U$ ages for the Xinan igneous rocks.

U–Pb dating (Table 3; Fig. 8) (Ballard et al., 2002; Liang et al., 2006). The Ce^{4+}/Ce^{3+} values of monzogranite (27 to 457, average: 231 ± 52 (2σ)), granodiorite porphyry (202 to 1706, average: 1078 ± 100 (2σ)), fine-grained granodiorite porphyry (239 to 1181, average: 793 ± 100 (2σ)), porphyritic granodiorite (264 to 1324, average: 729 ± 140 (2σ)) and aplite dyke (190 to 641, average: 414 ± 120 (2σ)) suggest that those of the ore-bearing granodiorite porphyry are higher and have a wider range than the barren granitoids.

5.4. In-situ zircon Hf isotope

Zircon Lu–Hf isotopes were determined for six samples with corresponding U–Pb dating on the same or similar domains of the zircon grains. The analytical results are listed in Table 4 and shown in Fig. 9. The $\varepsilon_{Hf}(t)$ values are calculated using their U–Pb ages (Table 4).

5.4.1. Monzogranite

Ten zircon Lu–Hf isotope analyses from the sample ZJ14XC046 yielded $^{176}Yb/^{177}Hf$ and $^{176}Hf/^{177}Hf$ values of 0.026953–0.056988 and 0.282397–0.282447, respectively, with low $^{176}Lu/^{177}Hf$ values of 0.000835 to 0.001740 (Table 4). ε_{Hf} (t) values range from −8.02 to −10.00, with the two-stage Hf model ages (T_{DM2}) varying from 1.72 to 1.84 Ga.

5.4.2. Granodiorite porphyry

Ten zircon Lu–Hf isotope analyses from the sample ZJ14XC036–958 yielded $^{176}Yb/^{177}Hf$ and $^{176}Hf/^{177}Hf$ values of 0.039369–0.066535 and 0.282536–0.282675, respectively, with low $^{176}Lu/^{177}Hf$ values of 0.001383 to 0.002272 (Table 4). $\varepsilon_{Hf}(t)$ values range from −1.15 to −6.05, with T_{DM2} varying from 1.24 to 1.56 Ga. Ten analyses from the sample ZJ14XC018 yielded $^{176}Yb/^{177}Hf$ and $^{176}Hf/^{177}Hf$ values of 0.044605–0.059128 and 0.282604–0.282666, respectively, with low $^{176}Lu/^{177}Hf$ values of 0.001391 to 0.001918 (Table 4). $\varepsilon_{Hf}(t)$ values range from −1.42 to −3.64, with T_{DM2} varying from 1.26 to 1.40 Ga.

5.4.3. Fine-grained granodiorite porphyry

Eight zircon Lu–Hf isotope analyses from the sample ZJ14XC039 yielded $^{176}Yb/^{177}Hf$ and $^{176}Hf/^{177}Hf$ values of 0.032063–0.055759 and 0.282592–0.282715, respectively, with $^{176}Lu/^{177}Hf$ values of 0.001133

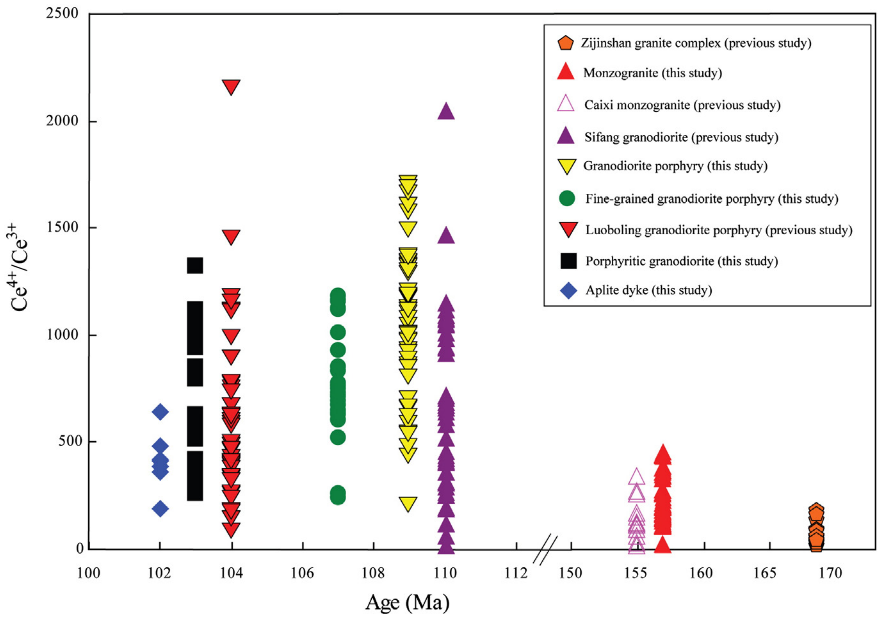

Fig. 8. Zircon Ce^{4+}/Ce^{3+} vs. U–Pb age diagram for the igneous rocks in the Zijinshan Orefield.

to 0.001974 (Table 4). $\varepsilon_{Hf}(t)$ values range from −4.08 to 0.32, with T_{DM2} varying from 1.15 to 1.43 Ga.

5.4.4. Porphyritic granodiorite

Ten zircon Lu–Hf isotope analyses from the sample ZK2418–907 yielded $^{176}Yb/^{177}Hf$ and $^{176}Hf/^{177}Hf$ values of 0.018812–0.029796 and 0.282650–0.282703, respectively, with $^{176}Lu/^{177}Hf$ values of 0.000706 to 0.001133 (Table 4). $\varepsilon_{Hf}(t)$ values range from −2.12 to −0.26, with T_{DM2} varying from 1.18 to 1.30 Ga.

5.4.5. Aplite dyke

Seventeen zircon Lu–Hf isotope analyses were performed for the sample ZJ14XC048. Seven U–Pb dated zircons (weighted average age = 102.3 ± 2.6 Ma) yielded $^{176}Yb/^{177}Hf$ and $^{176}Hf/^{177}Hf$ values of 0.019135–0.035255 and 0.282635–0.282729, respectively, with $^{176}Lu/^{177}Hf$ values of 0.000692 to 0.001197. $\varepsilon_{Hf}(t)$ values range from 0.66 to −2.72, with T_{DM2} varying from 1.12 to 1.34 Ga (Table 4).

Another seven U–Pb dated zircons (weighted average age of 141.1 ± 2.5 Ma) yielded $^{176}Yb/^{177}Hf$ and $^{176}Hf/^{177}Hf$ values of 0.025635–0.129183 and 0.282435–0.282573, respectively, with $^{176}Lu/^{177}Hf$ values of 0.000768 to 0.004076. $\varepsilon_{Hf}(t)$ values range from −4.07 to −8.85, with T_{DM2} varying from 1.45 to 1.76 Ga (Table 4).

Two zircons ($^{206}Pb/^{238}U$ ages: 160.0 ± 2.7 Ma and 159.0 ± 2.7 Ma) have $\varepsilon_{Hf}(t)$ values of −9.16 and −9.74, with T_{DM2} ages of 1.79 and 1.83 Ga, respectively. One old zircon ($^{206}Pb/^{238}U$ age: 840.0 ± 22.8 Ma) has $\varepsilon_{Hf}(t)$ value of −0.71, with T_{DM2} of 1.77 Ga.

6. Discussion

6.1. Timing of magmatism at the Xinan Cu–Mo deposit and the Zijinshan Orefield

Previous research suggested that the Zijinshan granite complex were emplaced during ca. 169–155 Ma (Zhao et al., 2008; Jiang et al., 2013; Huang, 2014; Li et al., 2015a). In this study, the two ca. 160 Ma inherited zircons from the aplite dyke were probably captured from the Zijinshan granite complex it intruded. Monzogranite occurs at depths at Xinan and in northeastern Zijinshan (e.g., the Caixi pluton, Fig. 1B), and has intruded the Zijinshan granite complex. Huang (2014) and Zhao et al. (2007) reported zircon U–Pb ages of 154.5 ± 4.7 Ma and 150 ± 3 Ma for the Caixi monzogranite, which are broadly coeval with our new zircon U–Pb age for the Xinan monzogranite (156.9 ± 1.0 Ma). Hence, we suggest that the monzogranite at Zijinshan was formed during ca. 157–150 Ma.

The ca. 110–102 Ma at Zijinshan had formed the Shimaoshan Group volcanic / pyroclastic sequences, including mainly rhyolite, dacite, andesite, ignimbrite and tuff (Yu et al., 2013; Jiang et al., 2013). The Sifang granodiorite (ca. 112–108 Ma) is distributed in northeastern Zijinshan (Fig. 1) and intruded into the Zijinshan granite complex (Mao et al., 2004a, b; Jiang et al., 2013; Huang, 2014). Recently, Zhong (2014) reported two zircon U–Pb ages of 107.1 ± 0.3 Ma and 106.9 ± 0.4 Ma for the Luoboling ore-bearing granodiorite porphyry. These ages are slightly older than those reported for the Luoboling ore-bearing granodiorite porphyry (103.8 ± 0.9 Ma and 98.1 ± 1.1 Ma; Huang, 2014), suggesting the magmatism was multi-episodic. The Xinan ore-bearing granodiorite porphyry (108.9 ± 1.0 Ma and 109.2 ± 0.9 Ma) may represent an even earlier episode for this granodioritic magmatism (ca. 109–98 Ma). Meanwhile, the barren Xinan fine-grained granodiorite porphyry (107.0 ± 0.8 Ma) suggests that not all granodiorite of this period are mineralized.

Barren porphyritic granodiorite occurs at depths beneath the ore-bearing granodiorite porphyries at Luoboling and Xinan. Yu et al. (2013) reported a zircon U–Pb age of 103 ± 2 Ma for the porphyritic granodiorite from the depths of Zijinshan epithermal Au–Cu deposit. Huang (2014) reported the similar zircon U–Pb age of 103.5 ± 1.0 Ma for the Luoboling porphyritic granodiorite, and another younger age of 98.1 ± 1.1 Ma, suggesting that the porphyritic granodiorite may have formed at two stages. Our new age attained for the Xinan porphyritic granodiorite (102.7 ± 0.7 Ma) is largely coeval with the ca. 103 Ma magmatic phase reported by Yu et al. (2013) and Huang (2014).

Some previous research argued that the Zijinshan Orefield experienced a 40 Ma magmatic quiescence at ca. 150–110 Ma (Jiang et al., 2013). However, the seven inherited zircons from the aplite dyke yielded a weighted average age of 141.1 ± 2.5 Ma, which may indicate possible earliest Cretaceous

Table 4
Zircon Lu–Hf isotopic data for the Xinan igneous rocks.

Sample spots	T(Ma)	$^{176}Yb/^{177}Hf$	σ	$^{176}Lu/^{177}Hf$	σ	$^{176}Hf/^{177}Hf$	σ	$\varepsilon_{Hf}(t)$	T_{DM2} (Ma)
Monzogranite									
ZJ14XC046–03	163	0.030174	0.000299	0.000923	0.000005	0.282447	0.000009	−8.02	1721
ZJ14XC046–04	161	0.026953	0.000246	0.000835	0.000004	0.282429	0.000008	−8.71	1762
ZJ14XC046–07	154	0.035191	0.000131	0.001051	0.000003	0.282435	0.000009	−8.66	1754
ZJ14XC046–08	157	0.038913	0.000392	0.001212	0.000015	0.282410	0.000007	−9.49	1809
ZJ14XC046–10	157	0.030964	0.000075	0.000980	0.000001	0.282427	0.000009	−8.87	1770
ZJ14XC046–11	157	0.041247	0.000163	0.001217	0.000004	0.282435	0.000008	−8.60	1753
ZJ14XC046–13	157	0.056988	0.001012	0.001740	0.000025	0.282421	0.000009	−9.15	1788
ZJ14XC046–16	155	0.042639	0.000184	0.001323	0.000005	0.282397	0.000008	−10.00	1839
ZJ14XC046–17	157	0.029808	0.000072	0.000906	0.000001	0.282427	0.000008	−8.84	1768
ZJ14XC046–18	157	0.042196	0.000132	0.001323	0.000001	0.282417	0.000008	−9.24	1793
Granodiorite porphyry									
ZJ14XC036–958-02	111	0.045896	0.000083	0.001588	0.000003	0.282642	0.000008	−2.28	1317
ZJ14XC036–958-04	110	0.047754	0.000366	0.001582	0.000012	0.282536	0.000009	−6.05	1556
ZJ14XC036–958-06	108	0.039369	0.000233	0.001383	0.000003	0.282622	0.000008	−3.02	1361
ZJ14XC036–958-07	108	0.051188	0.000746	0.001812	0.000022	0.282605	0.000008	−3.66	1402
ZJ14XC036–958-08	109	0.054941	0.000188	0.001931	0.000007	0.282626	0.000009	−2.93	1356
ZJ14XC036–958-10	107	0.066535	0.000402	0.002272	0.000011	0.282595	0.000008	−4.07	1427
ZJ14XC036–958-13	108	0.049690	0.000418	0.001779	0.000011	0.282624	0.000009	−3.00	1360
ZJ14XC036–958-16	109	0.041392	0.000217	0.001470	0.000003	0.282637	0.000009	−2.50	1330
ZJ14XC036–958-18	111	0.041307	0.000134	0.001488	0.000007	0.282588	0.000009	−4.18	1437
ZJ14XC036–958-20	111	0.054558	0.000291	0.001909	0.000008	0.282675	0.000008	−1.15	1244
Granodiorite porphyry									
ZJ14XC018–01	110	0.052402	0.000279	0.001718	0.000006	0.282611	0.000008	−3.42	1388
ZJ14XC018–03	113	0.057915	0.000154	0.001860	0.000004	0.282643	0.000007	−2.21	1314
ZJ14XC018–05	109	0.046133	0.000195	0.001499	0.000005	0.282604	0.000007	−3.64	1402
ZJ14XC018–06	112	0.052958	0.000717	0.001718	0.000016	0.282638	0.000009	−2.40	1325
ZJ14XC018–07	110	0.053510	0.000562	0.001733	0.000012	0.282626	0.000008	−2.86	1353
ZJ14XC018–10	113	0.044605	0.000514	0.001391	0.000008	0.282665	0.000008	−1.42	1263
ZJ14XC018–11	108	0.053925	0.001006	0.001674	0.000030	0.282629	0.000009	−2.79	1347
ZJ14XC018–14	109	0.058373	0.000212	0.001915	0.000004	0.282666	0.000008	−1.49	1265
ZJ14XC018–18	108	0.059128	0.000436	0.001918	0.000007	0.282666	0.000008	−1.50	1265
ZJ14XC018–23	109	0.051033	0.000440	0.001596	0.000011	0.282643	0.000008	−2.30	1317
Fine-grained granodiorite porphyry									
ZJ14XC039–02	109	0.033203	0.000427	0.001166	0.000011	0.282653	0.000008	−1.88	1290
ZJ14XC039–03	109	0.038090	0.000381	0.001318	0.000009	0.282592	0.000009	−4.08	1430
ZJ14XC039–04	109	0.040413	0.000099	0.001414	0.000003	0.282611	0.000009	−3.41	1387
ZJ14XC039–05	105	0.042309	0.000236	0.001534	0.000006	0.282667	0.000009	−1.50	1263
ZJ14XC039–06	107	0.055759	0.000372	0.001974	0.000015	0.282607	0.000009	−3.62	1399
ZJ14XC039–09	110	0.033258	0.000212	0.001175	0.000002	0.282715	0.000009	0.32	1151
ZJ14XC039–12	105	0.045026	0.000635	0.001601	0.000017	0.282624	0.000009	−3.05	1361
ZJ14XC039–13	108	0.052991	0.000559	0.001918	0.000022	0.282689	0.000009	−0.69	1213
ZJ14XC039–14	110	0.032063	0.000116	0.001133	0.000004	0.282625	0.000010	−2.85	1353
ZJ14XC039–16	106	0.032178	0.000164	0.001159	0.000003	0.282659	0.000008	−1.75	1280
Porphyritic granodiorite									
ZK2418–907-02	103	0.026855	0.000129	0.001018	0.000003	0.282650	0.000009	−2.12	1301
ZK2418–907-03	100	0.021057	0.000183	0.000796	0.000005	0.282672	0.000009	−1.41	1253
ZK2418–907-04	102	0.020301	0.000036	0.000750	0.000001	0.282671	0.000009	−1.40	1254
ZK2418–907-05	101	0.023180	0.000223	0.000870	0.000008	0.282664	0.000007	−1.65	1269
ZK2418–907-06	99	0.029796	0.000089	0.001133	0.000005	0.282693	0.000008	−0.70	1207
ZK2418–907-09	100	0.020197	0.000068	0.000733	0.000001	0.282687	0.000010	−0.88	1219
ZK2418–907-13	103	0.022985	0.000174	0.000869	0.000006	0.282653	0.000009	−2.01	1294
ZK2418–907-16	104	0.018812	0.000094	0.000706	0.000002	0.282683	0.000008	−0.91	1224
ZK2418–907-19	104	0.023109	0.000157	0.000822	0.000002	0.282688	0.000009	−0.76	1215
ZK2418–907-23	102	0.025826	0.000261	0.000962	0.000007	0.282703	0.000009	−0.26	1181
Aplite dyke									
ZJ14XC048–01	102	0.020541	0.000133	0.000744	0.000003	0.282729	0.000009	0.66	1123
ZJ14XC048–04	102	0.027700	0.000297	0.001017	0.000013	0.282655	0.000009	−1.97	1291
ZJ14XC048–05	160	0.114639	0.000737	0.003483	0.000017	0.282424	0.000010	−9.16	1790
ZJ14XC048–10	105	0.027814	0.000074	0.001014	0.000001	0.282687	0.000008	−0.79	1217
ZJ14XC048–08	138	0.093982	0.000750	0.002950	0.000031	0.282510	0.000008	−6.52	1606
ZJ14XC048–11	139	0.074786	0.000358	0.002305	0.000007	0.282505	0.000008	−6.60	1612
ZJ14XC048–12	840	0.045589	0.000310	0.001454	0.000008	0.282250	0.000011	−0.71	1772
ZJ14XC048–13	139	0.025635	0.000133	0.000768	0.000001	0.282573	0.000009	−4.07	1452
ZJ14XC048–14	103	0.034808	0.000675	0.001193	0.000020	0.282653	0.000010	−2.04	1295
ZJ14XC048–15	99	0.019135	0.000377	0.000692	0.000011	0.282635	0.000008	−2.72	1336
ZJ14XC048–17	101	0.022993	0.000189	0.000828	0.000007	0.282647	0.000009	−2.28	1309
ZJ14XC048–18	159	0.050685	0.000335	0.001568	0.000008	0.282403	0.000009	−9.74	1826
ZJ14XC048–19	145	0.030087	0.000717	0.000952	0.000020	0.282435	0.000008	−8.85	1760
ZJ14XC048–22	141	0.129183	0.000828	0.004076	0.000021	0.282516	0.000009	−6.33	1596

(continued on next page)

Table 4 (*continued*)

Sample spots	T(Ma)	$^{176}Yb/^{177}Hf$	σ	$^{176}Lu/^{177}Hf$	σ	$^{176}Hf/^{177}Hf$	σ	$\varepsilon_{Hf}(t)$	T_{DM2} (Ma)
ZJ14XC048-23	107	0.035255	0.000214	0.001197	0.000007	0.282674	0.000010	−1.20	1245
ZJ14XC048-24	144	0.072745	0.001643	0.002208	0.000061	0.282501	0.000008	−6.64	1618
ZJ14XC048-25	142	0.080203	0.000820	0.002394	0.000017	0.282477	0.000009	−7.53	1673

magmatism at Zijinshan, which is generally coeval with intensive magmatism and mineralization in the Middle–Lower Yangtze Metallogenic Belt (another significant Mesozoic mineralization province in the north of the Zijinshan district) of the South China (Zhou et al., 2015).

The Mesozoic (ca. 169–98 Ma) magmatism at Xinan (and Zijinshan Orefield as a whole) can be divided into two phases: (1) the Middle to Late Jurassic phase (ca. 169–150 Ma), forming the Zijinshan complex granite (ca. 169–155 Ma) and Xinan monzogranite (ca. 157–150 Ma); (2) The late Early Cretaceous phase (ca. 112–98 Ma), forming the Shimaoshan volcanic rocks (ca. 110–102 Ma), the Sifang granodiorite (ca. 112–108 Ma), together with the Xinan granodiorite porphyry (ca. 109–98 Ma), fine-grained granodiorite porphyry (ca. 107 Ma), porphyritic granodiorite (ca. 103–98 Ma) and aplite dykes (ca. 102 Ma). Additionally, a possible earliest Cretaceous magmatism (ca. 141 Ma) may also have existed based on the seven inherited zircons analyzed from the aplite dyke.

6.2. Implications of magmatic oxygen fugacity in porphyry mineralization

It is widely accepted that a genetic link exists between highly oxidized magma and porphyry mineralization (Arculus, 1994; Parkinson and Arculus, 1999; Ballard et al., 2002; Liang et al., 2006, 2009; Sillitoe, 2010). Sulfate (SO_4^{2-}) is over 10 times more soluble that sulfide (S^{2-}) in highly oxidized magmas (Sun et al., 2015), which favors metals (i.e., Cu, Au) enrichment in hydrothermal fluids and porphyry-related mineralization. Generally, high zircon Ce^{4+}/Ce^{3+} reflects high oxygen fugacity (fO_2), and ore-bearing porphyries commonly have high Ce^{4+}/Ce^{3+} (Ballard et al., 2002; Trail et al., 2011, 2012). Meanwhile, the generation of high fO_2 magmas may be associated with the incursion of highly oxidized slab-derived supercritical fluids into the lithospheric mantle, similar to the cases of the Central Andes (Bissig et al., 2003) and Halasu Cu belt in Eastern Junggar (NW China) (Wu et al., 2015). Ballard (2002) suggested that the progressive Ce^{4+}/Ce^{3+} increase is accompanied by increasing $(Eu/Eu^*)_N$ in zircons.

Huang (2014) proposed that the ore-bearing Luoboling granodiorite porphyry has higher zircon Ce^{4+}/Ce^{3+} than the barren intrusions, e.g., the Zijinshan granite complex and Caixi monzogranite (Fig. 8). Our and published data of the Zijinshan Orefield also demonstrate that the Middle to Late Jurassic granitoids (e.g., Zijinshan granite complex, Caixi monzogranite and Xinan monzogranite) have low Ce^{4+}/Ce^{3+} and thus relatively reduced magma, similar to the barren intrusions in northern Chile (Fig. 10) (Ballard et al., 2002). This conclusion is also supported by that the Middle to Late Jurassic granitoids lack magnetite as accessory mineral (Zhang et al., 2001; Li and Jiang, 2014). In contrast, zircon Ce^{4+}/Ce^{3+} values for the late Early Cretaceous to earliest Late Cretaceous ore-bearing porphyries are remarkably high, similar to the ore-forming Luoboling granodiorite porphyries (Figs. 8 and 10) (Sun et al., 2015; Wu et al., 2015). This, and the presence of accessory anhydrite and magnetite, suggest highly oxidized primary magmas for the Luoboling and Xinan ore-forming porphyries. The late Early Cretaceous aplite dyke has relatively low zircon Ce^{4+}/Ce^{3+}, suggesting its magma may have been fairly reduced. In the Ce^{4+}/Ce^{3+} vs. $(Eu/Eu^*)_N$ diagram (Fig. 10), the late Early Cretaceous to earliest Late Cretaceous Luoboling and Xinan ore-forming porphyries mainly fall in the fields of the ore-related intrusions in northern Chile, the El Teniente porphyry Cu–Mo deposit, and (partly overlapped with) the Dexing ore-bearing porphyry, suggesting all these rocks have comparable elevated oxygen fugacity ($Ce^{4+}/Ce^{3+} > 300$; Ballard et al., 2002; Muñoz et al., 2012; Zhang et al.,

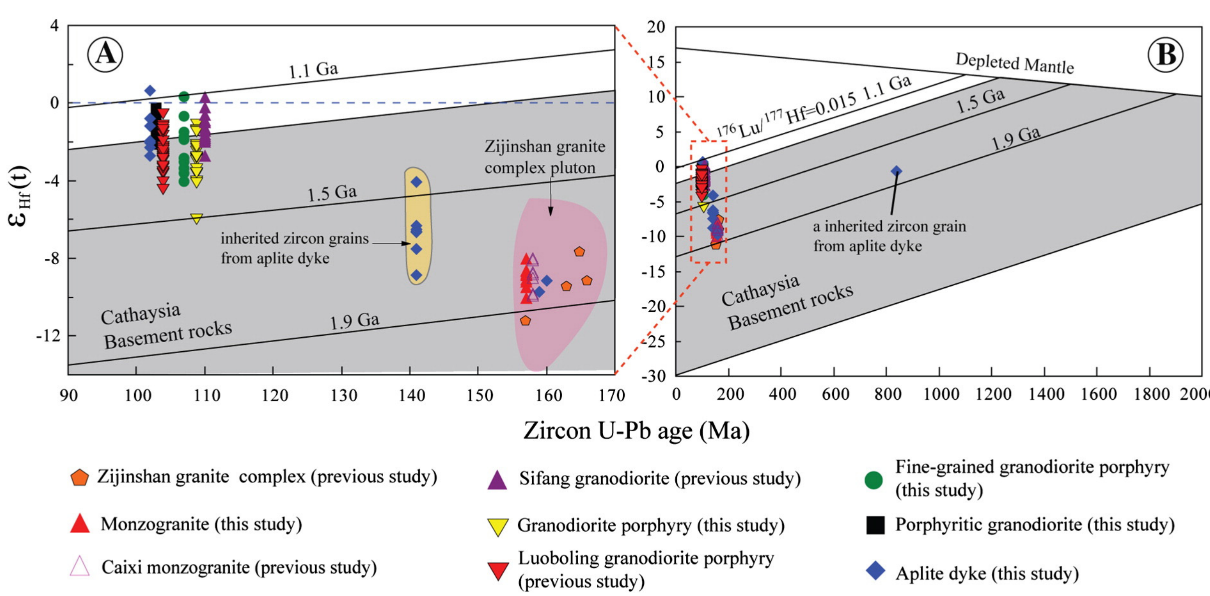

Fig. 9. Zircon εHf(t) vs. U–Pb age diagram for the igneous rocks in the Zijinshan Orefield. The gray field represents the Cathaysia basement data. The pink field represents the Zijinshan granite complex data. (For interpretation of the references to colour in this figure legend, the reader is referred to the web version of this article.)

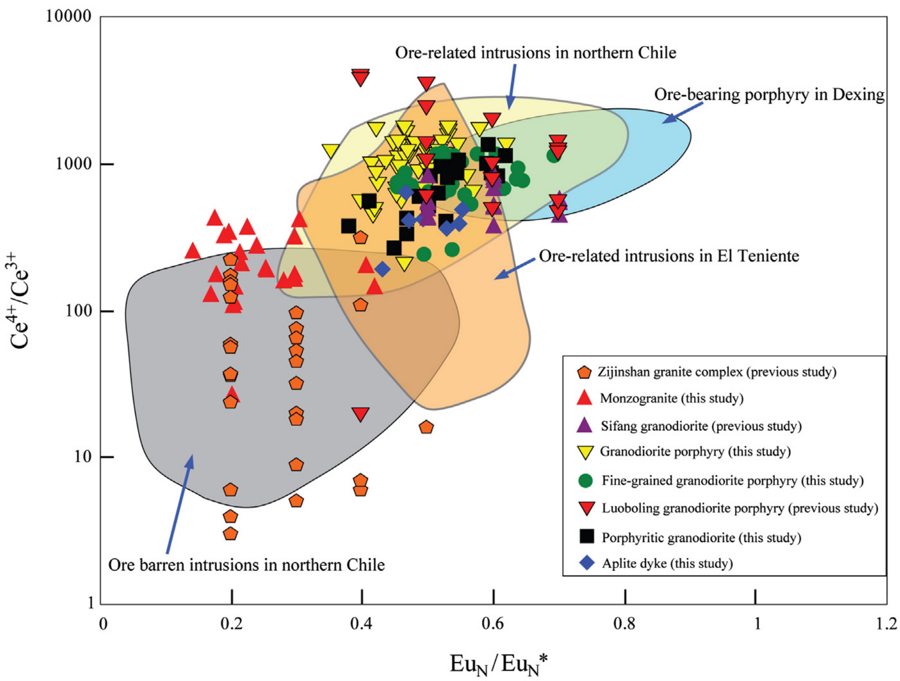

Fig. 10. Zircon Ce^{4+}/Ce^{3+} and $(Eu/Eu^*)_N$ ratios for the igneous rocks in the Zijinshan Orefield. Data of the ore-related / barren intrusions in northern Chile, El Teniente and Dexing are shown for comparison. The northern Chilean data (including the Pajonal–El Abra, Los Picos–Fortuna and the Chuquicamata suites) are from Ballard et al. (2002), El Teniente data are from Muñoz et al. (2012) and Dexing data are from Zhang et al. (2013).

2013). Thus, we suggest that the high fO_2 was a key controlling factor for the Zijinshan porphyry-related Au–Cu–Mo mineralization.

6.3. Petrogenesis and magma sources

6.3.1. Hydrothermal alteration and elements mobility

Base on petrographic observation and variable LOI values (below 3) listed in Table 2, all samples were carefully collected from the Xinan ore deposit in the Zijinshan Orefield and have undergone weak phyllic alteration without weathering (Fig. 3). So it is very necessary to evaluate the effects of hydrothermal alteration on major and trace elements of these samples prior to discuss petrogenesis, magma source and tectonic setting.

Zirconium is generally immobile under low-grade metamorphism and alteration (Guo et al., 2013; Ma et al., 2013). Hence, correlations between Zr and other elements can be used to evaluate element mobility in hydrothermal alteration processes (Polat et al., 2002; Liu et al., 2012). All the Xinan samples analyzed show poor correlation between Zr and LILEs (e.g., K and Rb; Fig. 11A and B), but good correlation between Zr and HSFEs (e.g., Nb; Fig. 11C), transition elements (e.g., Fe; Fig. 11D) and REEs (e.g., La, Sm, Eu, Y; Fig. 11E to H), suggesting that the HFSEs and REEs in the Xinan rocks are essentially immobile and can be used for petrogenetic interpretation.

6.3.2. Middle to late Jurassic magmatism

The Zijinshan granite complex is featured by high SiO_2 and K_2O, low MgO, TiO_2 and $Mg^\#$ (mostly <30), LREE/HREE enrichment ($(La/Yb)_N = 2.85$–18.54), strongly negative Eu anomalies and negative $\varepsilon_{Hf}(t)$ values (Jiang et al., 2013; Li et al., 2015a). The Zijinshan granite complex was interpreted to be generated from partial melting of the Paleoproterozoic metamorphosed Cathaysia Block crustal basement (Jiang et al., 2013; Liang et al., 2013). The Xinan monzogranite contains high SiO_2 and Al_2O_3, low MgO, $Mg^\#$ (36–39), Cr, Co and Ni (Table 2), suggesting a possible crustal source. The monzogranite shows positively correlated La vs. La/Sm (Fig. 12), suggesting that its compositional variation is mainly controlled by partial melting processes. In the Y vs. Sr/Y and Yb_N vs. $(La/Yb)_N$ diagrams (Fig. 13A, B), the Xinan monzogranite plots in the normal arc volcanics field, indicating a subduction-related origin. The Nb/Ta values of the monzogranite range from 10.88 to 13.87 (average = 12.26), similar to the average continental crust (12–13, Barth et al., 2000) and the crustal-derived Zijinshan complex granite (11.3–12.4, Jiang et al., 2013), resembling partial melting of dominant crustal-derived magmas. Combining the Hf isotopic evidence of the monzogranite ($\varepsilon_{Hf}(t) = -8.02$ to -10.00, $T_{DM2} = 1.72$ to 1.84 Ga), we suggest that the Zijinshan monzogranite was most likely to be derived from partial melting of the Paleoproterozoic metamorphosed Cathaysia Block crustal basement (Fig. 9). The medium Eu/Eu* (0.56–0.63) indicates that the rocks may have undergone weak plagioclase fractionation.

6.3.3. Late Early Cretaceous to earliest Late Cretaceous magmatism

The Xinan (fine-grained) granodiorite porphyry and porphyritic granodiorite have similar SiO_2, Al_2O_3 and MgO contents, $Mg^\#$ (average = 48), and relatively high Cr, Co and Ni (Table 2). The $Mg^\#$ value is similar to the Sifang granodiorite (average $Mg^\# = 48$, Zhao et al., 2007) and the Luoboling granodiorite porphyry (average $Mg^\# = 50$, Huang, 2014), suggesting more mantle involvement than the Middle to Late Jurassic magmatism. The rocks also display LILE and LREE enrichments and HREE and HFSE depletions, indicative of a subduction-related origin, as also supported by their low Sr/Y and $(La/Yb)_N$ but high Y and Yb_N (Fig. 13A, B), clearly distinctive from adakitic rocks (e.g., Los Pelambres ore-related porphyries, Reich et al., 2003; Dexing ore-related porphyries, Wang et al., 2015 and Yulong ore-related porphyries, Jiang et al., 2006) which are considered to be associated with porphyry deposits and probably formed by partial melting of subducted oceanic slab (Yang et al., 2005). Since the late Early Cretaceous to earliest Late Cretaceous intrusions are characterized by high fO_2, we propose that they are probably influenced by the slab-derived fluids, not the partial melting of slab. In addition, the Xinan (fine-grained) granodiorite porphyry and porphyritic granodiorite have similar Hf isotopic compositions with

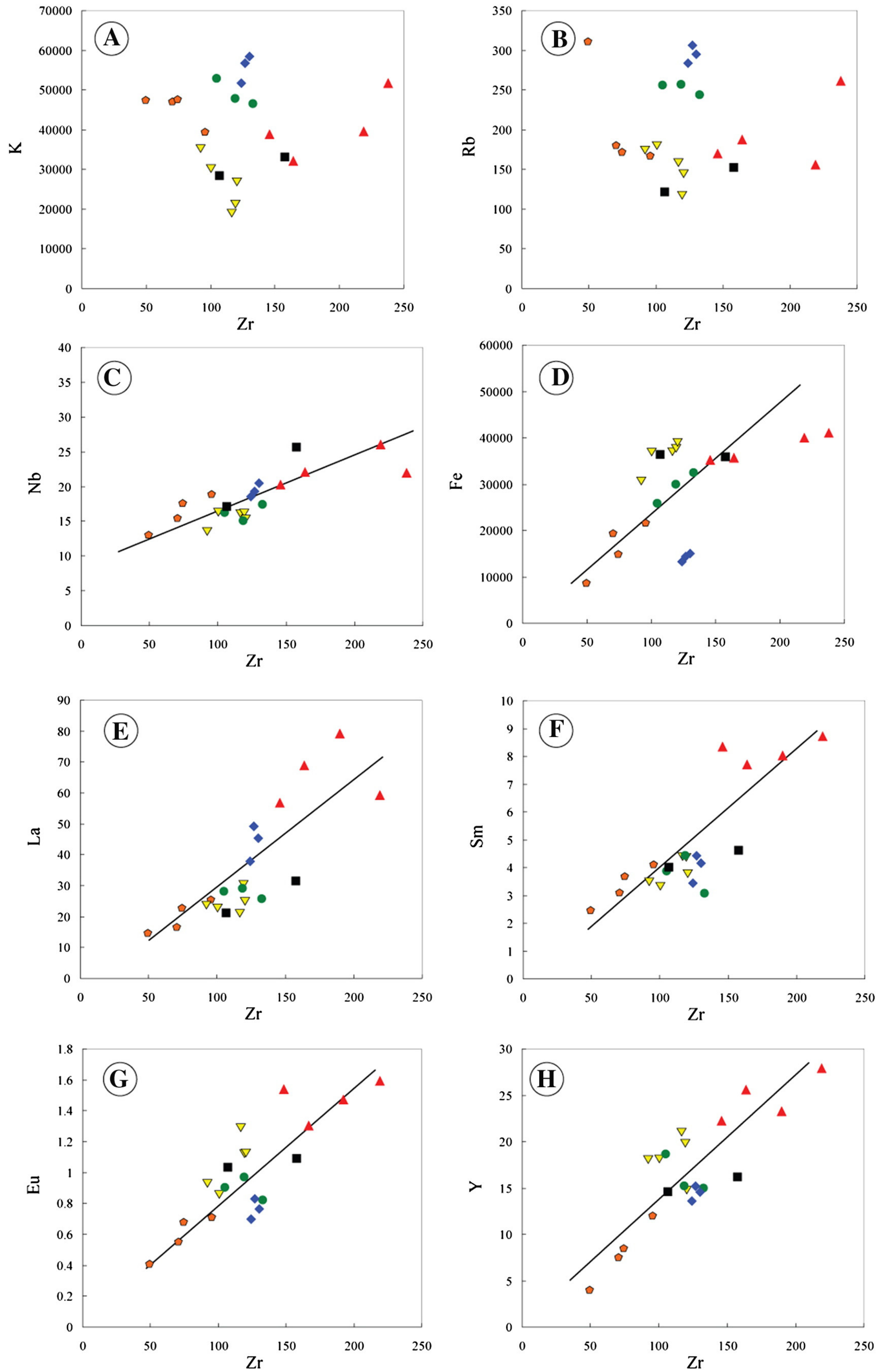

Fig. 11. A: Binary plots of whole-rock Zr vs. selected LILEs, HFSEs, transition elements and REEs. The Zijinshan complex granite data are from Zhang et al. (2001). Legends same as for Fig. 10.

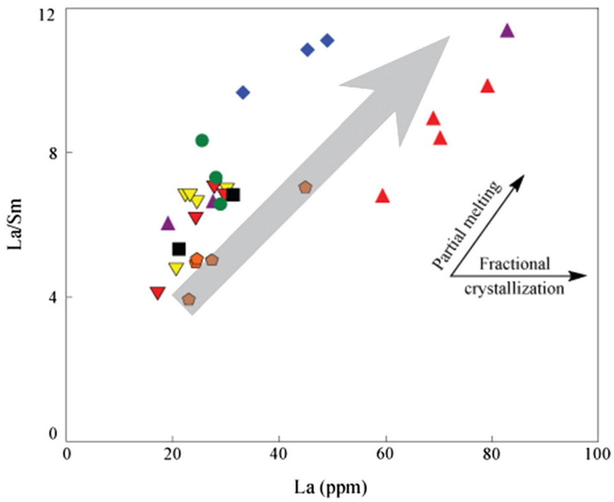

Fig. 12. La vs. (La/Sm) diagram after Pearce et al. (1984). Legends same as for Fig. 10.

the Sifang granodiorite ($\varepsilon_{Hf}(t) = 0.3$ to -2.7, $T_{DM2} = 1.15$ to 1.34 Ga, Zhong, 2014) and Luoboling granodiorite porphyry ($\varepsilon_{Hf}(t) = -5.6$ to 0.7, T_{DM2} = 1.10 to 1.49 Ga; Li and Jiang, 2015b), with their $\varepsilon_{Hf}(t)$ clearly higher than the Middle to Late Jurassic Zijinshan barren granitoids, indicating that they were mainly derived from the Mesoproterozoic metamorphosed Cathaysia Block crustal basement, but with more mantle and/or juvenile mafic lower crust involvements (Fig. 14). Moreover, the $\varepsilon_{Hf}(t)$ values of the Xinan and Luoboling ore-forming porphyries are distinctly lower than those reported from large porphyry deposits (Dexing, Wang et al., 2015; El Teniente, Muñoz et al., 2012; Yulong, Wang et al., 2011), suggesting that parental magmas of the former may have had fewer mantle inputs (Fig. 14). Their relatively low Nb/Ta may have been caused by the presence of residual rutile in the primary magma (Green, 1995), and their subtle Eu anomalies suggest minor plagioclase fractionation.

The late aplite dyke shares some geochemical and isotopic similarities with the (fine-grained) granodiorite porphyry and porphyritic granodiorite, including similar $\varepsilon_{Hf}(t)$ (Figs. 9 and 14), trace elements and REE patterns (Fig. 5), which probably reflect similar magma source. However, the aplite dykes contain higher Nb/Ta (11.44–12.87), SiO_2 and Al_2O_3 contents, and lower $Mg^{\#}$ (average = 30), implying more crustal involvements during the magma emplacement, as also evidenced by the presence of multiple generations of inherited zircons (ca. 141 Ma, 160 Ma and 840 Ma) in the dykes. The aplite dykes also show lower Eu/Eu* (0.60–0.64), higher LREE/HREE, and negative Nb, Ta and Ti anomalies, indicative of hornblende, rutile and plagioclase fractionation.

6.4. Tectonic and metallogenic implications

6.4.1. Tectonic setting

Mesozoic tectonic setting of the SE China coastal area (including the Zijinshan Orefield) is variably argued to be: (1) lithospheric extension (Li, 2000; Li et al., 2003; Wang et al., 2008; Chen et al., 2008); and (2) Pacific plate subduction (Zhou and Li, 2000; Pirajno and Bagas, 2002; Li and Li, 2007; Sun. et al., 2007; Wang et al., 2013).

Paleomagnetic and tectonic analyses suggested that SE China was affected by the Pacific plate subduction since the Middle Jurassic (ca. 180–170 Ma) (Zhao et al., 2004; Dong et al., 2007; Jiang et al., 2009; He et al., 2010; Li et al., 2015a). More recently, Li et al. (2016) argued that the subduction may have commenced in the Triassic (ca. 242 Ma), as indicated by geochemical and Sr–Nd–Pb–Hf isotopic compositions of the granodiorites north of Zijinshan. Geochemical data of the Xinan granitoids (enrichment of LILEs and LREEs and depletion of HFSEs) also indicate a subduction-related setting in the Middle to Late Jurassic and late Early Cretaceous to earliest Late Cretaceous (Fig. 5). Combine all those above, we summarize that the reasonable Mesozoic tectonic setting of the coastal SE China (including Zijinshan) is under the Pacific plate subduction setting.

In addition, Middle to Late Jurassic (ca. 175–150 Ma) peraluminous S-type granitic magmatism was widespread along the SE China coast, as also supported by the Zijinshan Hf isotope data, which suggest that these granitoids were mostly derived from partial melting of crustal materials, implying a compressive tectonic setting (Li et al., 2015a). Recently, Li and Jiang (2014, 2015b) proposed that asthenospheric mantle source may have contributed to the late Early Cretaceous granite petrogenesis, based on initial Pb and Hf isotopic evidence. The generation of these granitoids was associated with the Pacific plate subduction in an extensional setting during the Cretaceous. Meanwhile, our whole-rock geochemistry and Hf isotope data indicate that parental magma of the late Early Cretaceous to earliest Late Cretaceous granitoids (ca. 112–98 Ma) were also likely to be Pacific subduction-related. Furthermore, multi-stage Early Cretaceous (ca. 137–122 Ma, Yang et al., 2010; ca. 110–101 Ma, Li, 2000) A-type granitoids are widespread in South China, also suggesting an extensional setting. Consequently, we conclude that the Zijinshan magmatism and porphyry-related Au–Cu–Mo mineralization may

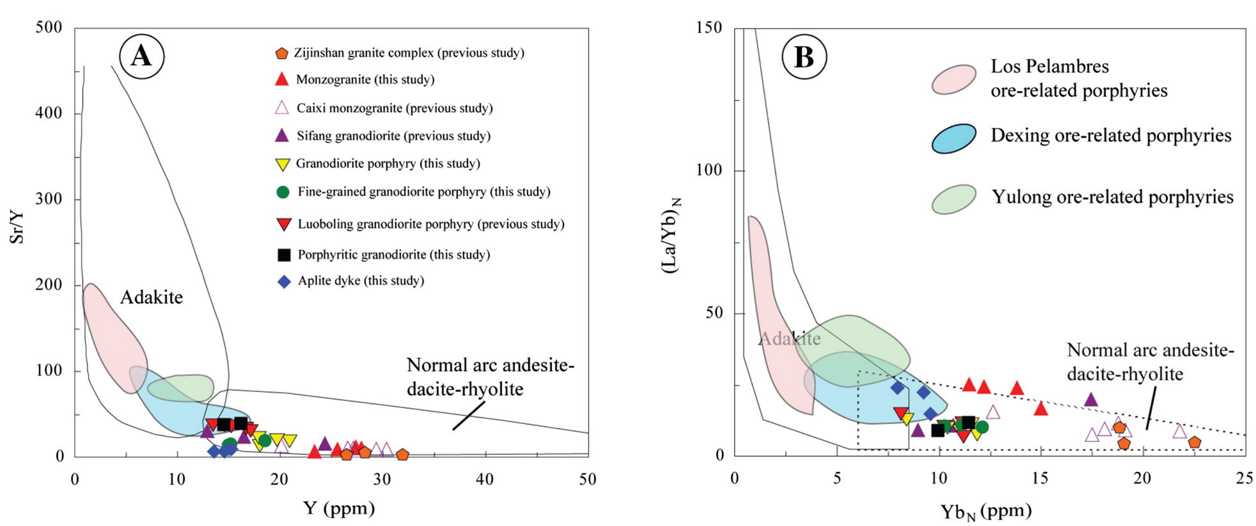

Fig. 13. (A) Y vs. Sr/Y and (B) Yb_N vs. $(La/Yb)_N$ diagrams for the igneous rocks in the Zijinshan Orefield. The diagrams are modified after Defant and Drummond (1990, 1993). Ore-related porphyries data of Los Pelambres (Reich et al., 2003), Dexing (Wang et al., 2015) and Yulong (Jiang et al., 2006) are shown for comparison.

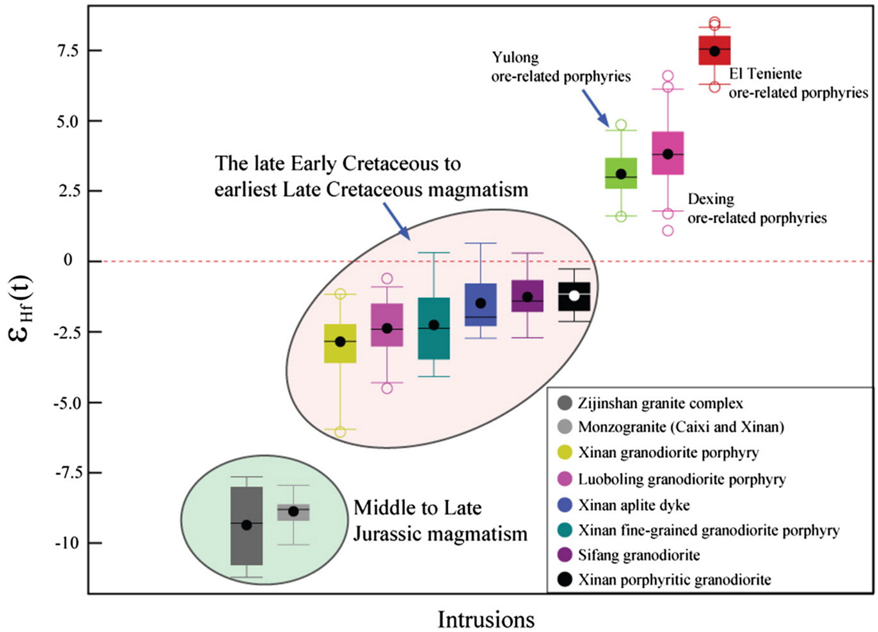

Fig. 14. Comparison of $\varepsilon_{Hf}(t)$ values between the Middle to Late Jurassic and the late Early Cretaceous to earliest Late Cretaceous granitoids in the Zijinshan Orefield. Ore-related porphyries from world-class porphyry deposits are also shown for comparison. Data of El Teniente, Dexing and Yulong are from Muñoz et al. (2012), Wang et al. (2015) and Wang et al. (2011), respectively.

have occurred under an extensional tectonic regime related to the late Early Cretaceous Pacific plate subduction.

The compressive to extensional/transtensional tectonic transition in the SE China coastal region may have been linked to the change in subduction direction (Koppers et al., 2001; Sharp and Clague, 2006; Sun. et al., 2007) from northwest to north, led by the formation of the Ontong Java Plateau (ca. 125–110 Ma; Larson, 1991; Maruyama et al., 1997; Smith, 2007). Such subduction direction changes may have caused a slab window-opening and/or rollback of the subducting Pacific Plate for asthenospheric upwelling, forming the relatively high $\varepsilon_{Hf}(t)$ found in the Zijinshan Orefield magmatic rocks (e.g., Li et al., 2015b).

To summarize, we propose that: (1) in the Middle to Late Jurassic (ca. 169–150 Ma), the Pacific plate may have subducted beneath SE China, with a general compressive tectonic regime exerted to the latter. This may have caused the partial melting of Paleoproterozoic Cathaysia Block basement to form the Zijinshan granite complex and monzogranite in the Zijinshan Orefield (Fig. 15A). (2) In the late Early Cretaceous to earliest Late Cretaceous, the slab window-opening (ca. 125–115 Ma) and rollback (ca. 115–98 Ma) of the subducting Pacific plate (following the subduction direction change) may have led to local extension and asthenospheric upwelling in the Zijinshan Orefield. Subsequently, the highly oxidized slab-derived supercritical fluids and the asthenospheric upwelling may have triggered the partial melting of the enriched lithospheric mantle and produced the water-rich and highly oxidized primary magma. This magma may have ascended to generate partial melting of the Mesoproterozoic Cathaysia Block basement accompanying with mantle and / or mafic lower crust involvement to form the Sifang granodiorite, Luoboling granodiorite porphyry, Xinan (fine-grained) granodiorite porphyry and porphyritic granodiorite, together with the associated Zijinshan porphyry-related Au–Cu–Mo mineralization. The late aplite dykes may have been the more crustal contaminated and fractionated products of this magma (Fig. 15B).

6.4.2. Gold–Cu–Mo metallogeny

The alunite Ar–Ar ages from the Zijinshan high-sulfidation epithermal Au–Cu deposit were interpreted to represent the mineralization age (ca. 112–104 Ma) (Zhang et al., 1991; Zhong, 2014). The hydrothermal biotite Ar–Ar ages and molybdenite Re–Os isochron ages indicated that the Luoboling porphyry deposit was formed during ca. 105–103 Ma (Zhang et al., 2005; Liang et al., 2012; Zhong, 2014). Our unpublished molybdenite Re–Os age (ca. 108 Ma) for the Xinan Cu–Mo deposit is largely coeval with the Xinan ore-forming granodiorite porphyry. Hence, we conclude that the porphyry-related Au–Cu–Mo mineralization in the Zijinshan Orefield mainly occurred in the late Early Cretaceous.

To further understand the ore genesis of the porphyry deposits in the Zijinshan Orefield, we have chosen typical world-class porphyry Cu–Mo deposits, including porphyry deposits in the Andes (El Teniente and Los Pelambres), Dexing and Yulong (China) to compare with porphyry deposits in the Zijinshan Orefield (Luoboling and Xinan ore deposit). The ore-related intrusions of the typical giant porphyry deposits show high Sr/Y geochemical characteristics and they have generally been considered to be formed by partial melting of metasomatized mantle wedge with high $\varepsilon_{Hf}(t)$ values (Richards, 2003; Zhou et al., 2015). However, the ore-related intrusions in the Zijinshan Orefield belong to subduction-related magmatic rocks without high Sr/Y feature (Fig. 13), and their $\varepsilon_{Hf}(t)$ values are lower than the ore-forming porphyries of world-class porphyry deposits (Fig. 14), implying that the nature of ore-related magma at Zijinshan is different, though the ore-related intrusions in the Zijinshan Orefield show similar high fO_2 primary magma with those of the typical porphyry deposits (Fig. 10). Such distinct nature of magma source is probably the vital factor for the relatively weak porphyry-type mineralization at the Zijinshan Orefield compared to the world-class porphyry Cu–Mo (–Au) deposit.

7. Conclusions

(1) Mesozoic magmatism in the Zijinshan Orefield includes a Middle to Late Jurassic (ca. 169–150 Ma) phase and a late Early Cretaceous to earliest Late Cretaceous (ca. 112–98 Ma) phase. An earliest Cretaceous (ca. 141 Ma) phase may have also existed based on inherited zircon data.

(2) All the Mesozoic Zijinshan igneous rocks may have been subduction-related and lack high Sr/Y signature. The Middle to Late Jurassic granitoids may have been partial melting products of the Paleoproterozoic metamorphosed Cathaysia Block basement,

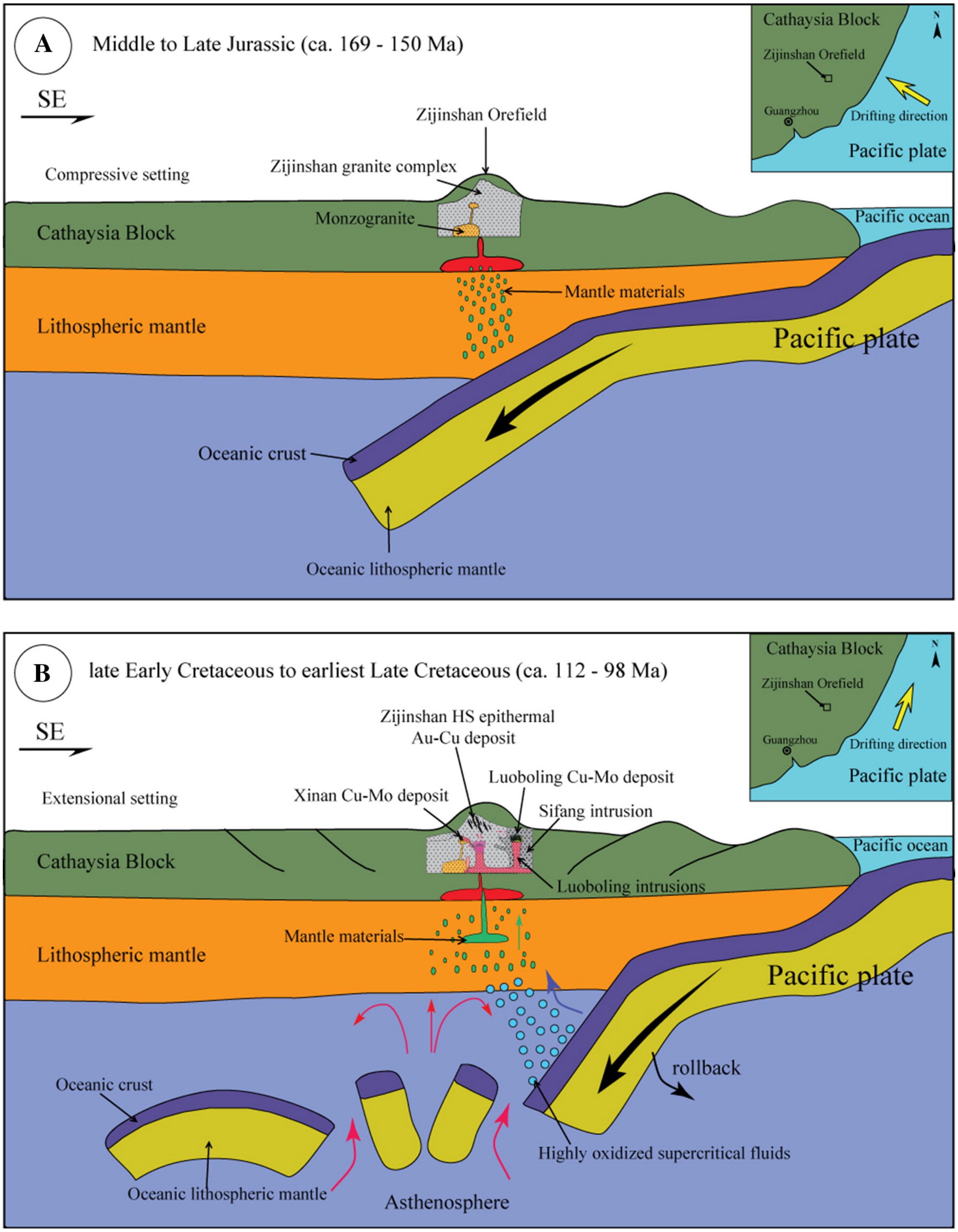

Fig. 15. Schematic tectonic model for the Mesozoic magmatism and mineralization of the Zijinshan Orefield, modified from Sun. et al. (2007), Jiang et al. (2013) and Huang (2014). See text for details.

whereas the late Early Cretaceous to earliest Late Cretaceous ones were likely to be derived also from partial melting of the basement but with more mantle and/or juvenile mafic lower crustal input. Their primary magmas may have had high fO_2, which is favorable to porphyry Cu mineralization.

(3) During the Middle to Late Jurassic, the Zijinshan Orefield may have been in a compressive setting caused by the Pacific plate subduction beneath SE China. The extensional tectonics in the late Early Cretaceous to earliest Late Cretaceous may have been caused by the subduction direction change (from NE to north) and rollback and slab window-opening.

(4) Tectonic regime transition, high fO_2 and the incorporation of the mantle/mafic lower crustal materials in the late Early Cretaceous to earliest Late Cretaceous may have been instrumental in forming the Zijinshan porphyry-related Au–Cu–Mo mineralization. But the distinct nature of magma source (without high Sr/Y) may have been vital factor for preventing the porphyry deposits in the Zijinshan Orefield to be the high grade world-class deposits.

Acknowledgements

This research was financially supported by the Creative and Interdisciplinary Program, CAS (Y433131A07) and the Natural Science Foundation of China (41502073). Field work was assisted by the Zijin Mining Group Co. Ltd. and its geologists, in particular Yuchuan Luo, Qing Wang and Lin Luo. Dr. Congying Li from the Key Laboratory of Mineralogy and Metallogeny (GIG CAS) is thanked for assisting the laboratory work. Prof. Noel White and Dr. Bing Xiao are thanked for their useful discussions and suggestions. We also thank guest editor Dr. Yanhua Zhang, and reviewers Dr. Jianwei Zi and Prof. Shaoyong Jiang for their relevant comments and constructive suggestions, which considerably improved the manuscript. This is contribution no. IS-2259 from GIGCAS.

References

Arculus, R.J., 1994. Aspects of magma genesis in arcs. Lithos 33, 189–208.
Ballard, J.R., Palin, M.J., Campbell, I.H., 2002. Relative oxidation states of magmas inferred from Ce (IV) / Ce (III) in zircon: application to porphyry copper deposits of northern Chile. Contrib. Mineral. Petrol. 144, 347–364.
Barth, M.G., McDonough, W.F., Rudnick, R.L., 2000. Tracking the budget of Nb and Ta in the continental crust. Chem. Geol. 165, 197–213.
Bissig, T., Clark, A.H., Lee, J.K.W., Quadt, A.V., 2003. Petrogenetic and metallogenetic responses to Miocene slab flattening: new constraints from the El Indio-Pascua Au–Ag–Cu belt, Chile/Argentina. Mineral. Deposita 38, 844–862.
Black, L.P., Kamo, S.L., Allen, C.M., Aleinikoff, J.N., Davis, D.W., Korsch, R.J., Foudoulis, C., 2003. TEMORA 1: a new zircon standard for Phanerozoic U–Pb geochronology. Chem. Geol. 200, 155–170.
Bouvier, A., Vervoort, J.D., Patchett, P.J., 2008. The Lu–Hf and Sm–Nd isotopic composition of CHUR: constraints from unequilibrated chondrites and implications for the bulk composition of terrestrial planets. Earth Planet. Sci. Lett. 273, 48–57.
Chen, C.H., Lee, C.Y., Shinjo, R.I., 2008. Was there Jurassic paleo-Pacific subduction in South China?: constraints from ^{40}Ar–^{39}Ar dating, elemental and Sr-Nd-Pb isotopic geochemistry of the Mesozoic basalts. Lithos 106, 83–92.
Chen, J., Chen, Y.J., Zhong, J., Sun, Y., Li, J., Qi, J.P., Lu, Y.H., 2011. Fluid inclusion study of the Wuziqilong Cu deposit in the Zijinshan ore field, Fujian Province. Acta Petrol. Sin. 27, 1425–1438 (in Chinese with English abstract).
Chen, Y.J., Chen, H.Y., Zaw, K., Pirajno, F., Zhang, Z.J., 2007. Geodynamic settings and tectonic model of skarn gold deposits in China: an overview. Ore Geol. Rev. 31, 139–169.
Cooke, D.R., Hollings, P., Walshe, J.L., 2005. Giant porphyry deposits: characteristics, distribution, and tectonic controls. Econ. Geol. 100, 801–818.
Defant, M.J., Drummond, M.S., 1990. Derivation of some modern arc magmas by melting of young subducted lithosphere. Nature 347, 662–665.
Defant, M.J., Drummond, M.S., 1993. Mount St. Helens; potential example of the partial melting of the subducted lithosphere in a volcanic arc. Geology 21, 547–550.
Dong, S.W., Zhang, Y.Q., Long, C.X., Yang, Z.Y., Ji, Q., Wang, T., Hu, J.M., Chen, X.H., 2007. Jurassic tectonic revolution in China and new interpretation of the Yanshan movement. Acta Geol. Sin. 11, 1449–1461 (in Chinese with English abstract).
Guo, R.R., Liu, S.W., Santosh, M., Li, Q.G., Bai, X., Wang, W., 2013. Geochemistry, zircon U–Pb geochronology and Lu–Hf isotopes of metavolcanics from eastern Hebei reveal Neoarchean subduction tectonics in the North China Craton. Gondwana Res. 24, 664–686.
Griffin, W.L., Wang, X., Jackson, S.E., Pearson, N.J., O'Reilly, S.Y., Xu, X.S., Zhou, X.M., 2002. Zircon chemistry and magma mixing, SE China: in-situ analysis of Hf isotopes, Tonglu and Pingtan igneous complexes. Lithos 61, 237–269.
Green, T.H., 1995. Significance of Nb/Ta as an indicator of geochemical processes in the crust–mantle system. Chem. Geol. 120, 347–359.
Hastie, A.R., Kerr, A.C., Pearce, J.A., Mitchell, S.F., 2007. Classification of altered volcanic island arc rocks using immobile trace elements: development of the Th–Co discrimination diagram. J. Petrol. 48 (12), 2341–2357.
He, Z.Y., Xu, X.S., Niu, Y.L., 2010. Petrogenesis and tectonic significance of a Mesozoic granite–syenite–gabbro association from inland South China. Lithos 119, 621–641.
Hu, C.J., Huang, W.T., Bao, Z.W., Liang, H.Y., Wang, C.L., 2012. LA–ICP–MS Zircon U–Pb Dating of the Dacite Porphyry from Zijinshan Cu-Au Deposit and its Metallogenetic Implications. Geotecton. Metallog. 36 (2), 284–292 (in Chinese with English abstract).
Huang, W.T., Li, J., Liang, H.Y., Wang, C.L., Lin, S.P., Wang, X.Z., 2013. Zircon LA-ICP-MS U–Pb ages and highly oxidized features of magma associated with Luoboling porphyry Cu–Mo deposit in Zijinshan ore field, Fujian Province. Acta Petrol. Sin. 29, 283–293 (in Chinese with English abstract).
Huang, W.T., 2014. Magmatism and Mineralization in the Zijinshan–Luoboling Ore-Field, Fujian Province, China. Guangzhou Institute of Geochemistry, Chinese Academy of Sciences, Guangzhou (pH.D. Thesis).
Hsü, K.J., Sun, S., Chen, H.H., Pen, H.H., Sengor, A.M.C., 1988. Mesozoic overthrust tectonics in South China. Geology 16, 418–421.
Jiang, Y.H., Jiang, S.Y., Ling, H.F., Dai, B.Z., 2006. Low-degree melting of a metasomatized lithospheric mantle for the origin of Cenozoic Yulong monzogranite-porphyry, East Tibet: geochemical and Sr–Nd–Pb–Hf isotopic constraints. Earth Planet. Sci. Lett. 241, 617–633.
Jiang, Y.H., Jiang, S.Y., Dai, B.Z., Liao, S.Y., Zhao, K.D., Ling, H.F., 2009. Middle to late Jurassic felsic and mafic magmatism in southern Hunan province, southeast China: Implications for a continental arc to rifting. Lithos 107 (3), 185–204.
Jiang, S.H., Liang, Q.L., Bagas, L., Wang, S.H., Nie, F.J., Liu, Y.F., 2013. Geodynamic setting of the Zijinshan porphyry–epithermal Cu–Au–Mo–Ag ore system, SW Fujian Province, China: constraints from the geochronology and geochemistry of the igneous rocks. Ore Geol. Rev. 53, 287–305.
Koppers, A.A.P., Morgan, J.P., Morgan, J.W., Staudigel, H., 2001. Testing the fixed hotspot hypothesis using $^{40}Ar/^{39}Ar$ age progressions along seamount trails. Earth Planet. Sci. Lett. 185, 237–252.
Larson, R.L., 1991. Latest pulse of earth: evidence for a mid-cretaceous superplume. Geology 19, 547–550.
Li, B., Zhao, K.D., Yang, S.Y., Dai, B.Z., 2013. Petrogenesis of the porphyritic dacite from Ermiaogou Cu–Au deposit in Zijinshan ore field and its metallogenetic implications. Acta Petrol. Sin. 29, 4167–4185 (in Chinese with English abstract).
Li, B., Jiang, S.Y., 2014. Geochronology and geochemistry of cretaceous Nanshanping alkaline rocks from the Zijinshan district in Fujian Province, South China: implications for crust - mantle interaction and lithospheric extension. J. Asian Earth Sci. 93, 253–274.
Li, B., Zhao, K.D., Zhang, Q., Xu, Y.M., Zhu, Z.Y., 2015a. Petrogenesis and geochemical characteristics of the Zijinshan granitic complex from Fujian Province, South China. Acta Petrol. Sin. 31, 811–828 (in Chinese with English abstract).
Li, B., Jiang, S.Y., 2015b. A subduction-related metasomatically enriched mantle origin for the Luoboling and Zhongliao cretaceous granitoids from South China: implications for magma evolution and Cu–Mo mineralization. Int. Geol. Rev. 57 (9–10), 1239–1266.
Li, B., Jiang, S.Y., Zhang, Q., Zhao, H.X., Zhao, K.D., 2015b. Cretaceous crust-mantle interaction and tectonic evolution of Cathaysia block in South China: evidence from pulsed mafic rocks and related magmatism. Tectonophysics 661, 136–155.
Li, B., Jiang, S.Y., Zhang, Q., Zhao, H.X., Zhao, K.D., 2016. Geochemistry, geochronology and Sr–Nd–Pb–Hf isotopic compositions of Middle to Late Jurassic syenite–granodiorites–dacite in South China: petrogenesis and tectonic implications. Gondwana Res. http://dx.doi.org/10.1016/j.gr.2015.05.006.
Li, X.H., 2000. Cretaceous magmatism and lithospheric extension in Southeast China. J. Asian Earth Sci. 18, 294–305.
Li, X.H., Chen, Z.G., Liu, D.Y., Li, W.X., 2003. Jurassic gabbro-granite-syenite suites from southern Jiangxi Province (SE China): age, origin and tectonic significance. Int. Geol. Rev. 45, 898–921.
Li, Z.X., Li, X.H., 2007. Formation of the 1300-km-wide intracontinental orogen and postorogenic magmatic province in Mesozoic South China: a flat-slab subduction model. Geology 35, 179–182.
Liang, H.Y., Campbell, I.H., Allen, C., Sun, W.D., Liu, C.Q., Yu, H.X., Xie, Y.W., Zhang, Y.Q., 2006. Zircon Ce^{4+} / Ce^{3+} ratios and ages for Yulong ore-bearing porphyries in eastern Tibet. Mineral. Deposita 41, 152–159.
Liang, H.Y., Sun, W., Su, W.C., Zartman, R.E., 2009. Porphyry copper-gold mineralization at Yulong, China, promoted by decreasing redox potential during magnetite alteration. Econ. Geol. 104, 587–596.
Liang, Q.L., Jiang, S.H., Wang, S.H., Li, C., Zeng, F.G., 2012. Re–Os dating of molybdenite from the Luoboling porphyry Cu–Mo deposit in the Zijinshan orefield of Fujian Province and its geological significance. Acta Geol. Sin. 86, 1113–1118 (in Chinese with English abstract).
Liang, Q.L., Jiang, S.H., Wang, S.H., Liu, Y.F., Bai, D.M., Chen, C.L., 2013. Petrogenesis of the Mesozoic magmatic rocks in Zijinshan area: constraints from zircon Hf isotope evidence. Acta Petrol. Mineral. 32, 318–328 (in Chinese with English abstract).
Liu, S.W., Zhang, J., Li, Q.G., Zhang, L.F., Wang, W., Yang, P.T., 2012. Geochemistry and U–Pb zircon ages of metamorphic volcanic rocks of the Paleoproterozoic Lüliang complex and constraints on the evolution of the Trans-North China orogen, North China Craton. Precambrian Res. 222–223, 173–190.
Liu, Y.S., Hu, Z.C., Gao, S., Guenther, D., Xu, J., Gao, C.G., Chen, H.H., 2008. In situ analysis of major and trace elements of anhydrous minerals by LA-ICP-MS without applying an internal standard. Chem. Geol. 257, 34–43.
Liu, Y.S., Gao, S., Hu, Z.C., Gao, C.G., Zong, K.Q., Wang, D.B., 2010. Continental and oceanic crust recycling-induced melt-peridotite interactions in the Trans-North China orogen: U–Pb dating, Hf isotopes and trace elements in zircon grains from mantle xenoliths. J. Petrol. 51, 537–571.
Ludwig, K.R., 2003. Isoplot/Ex, Version 3.0: A Geochronological Toolkit for Microsoft Excel. Geochronology Center, Berkeley, Special Publication.
Ma, L., Wang, Q., Wyman, D.A., Jiang, Z.Q., Yang, J.H., Li, Q.L., Gou, G.N., Guo, H.F., 2013. Late cretaceous crustal growth in the Gangdese area, southern Tibet: petrological and Sr–Nd–Hf–O isotopic evidence from Zhengga diorite–gabbro. Chem. Geol. 349, 54–70.
Mao, J.R., Tao, K.Y., Li, J.Y., Xie, F.G., Xu, N.Z., 2002. Geochronology and geochemical characteristics in late Mesozoic Sifang pluton, southwestern Fujian, and their significance. Acta Petrol. Sin. 18, 449–458 (in Chinese with English abstract).
Mao, J.R., Xu, N.Z., Hu, Q., Xing, G.F., Yang, Z.L., 2004b. The Mesozoic rock-forming and ore-forming processes and tectonic environment evolution in Shanghai-Datian region, Fujian. Acta Petrol. Sin. 20 (2), 285–296 (in Chinese with English abstract).
Mao, J.W., Xie, G.Q., Li, X.F., Zhang, C.Q., Mei, Y.X., 2004a. Mesozoic large scale mineralization and multiple lithospheric extension in South China. Earth Sci. Front. 11, 45–55 (in Chinese with English abstract).
Maruyama, S., Isozatggki, Y., Kimura, G., Terabayashi, M., 1997. Paleogeographic maps of the Japanese islands: plate tectonic synthesis from 750 Ma to the present. Island Arc 6, 121–142.
Muñoz, M., Charrier, R., Fanning, C.M., Maksaev, V., Deckart, K., 2012. Zircon trace element and O–Hf isotope analyses of mineralized intrusions from el Teniente ore deposit, Chilean Andes: constraints on the source and magmatic evolution of porphyry Cu–Mo related magmas. J. Petrol. 1091–1122.
Parkinson, I.J., Arculus, R.J., 1999. The redox state of subduction zones: insights from arc-peridotites. Chem. Geol. 160, 409–423.

Pearce, J.A., Harris, N.B.W., Tindle, A.G., 1984. Trace element discrimination diagrams for the tectonic interpretation of granitic rocks. J. Petrol. 25, 956–983.
Pirajno, F., Bagas, L., 2002. Gold and silver metallogeny of the South China Fold Belt: a consequence of multiple mineralizing events? Ore Geol. Rev. 20, 109–126.
Pirajno, F., Zhou, T.F., 2015. Intracontinental porphyry and porphyry-skarn mineral Systems in Eastern China: scrutiny of a special case "made-in-China". Econ. Geol. 110, 603–629.
Polat, A., Hofmann, A.W., Rosing, M.T., 2002. Boninite-like volcanic rocks in the 3.7-3.8 Ga Isua greenstone belt, West Greenland: geochemical evidence for intra-oceanic subduction zone processes in the early earth. Chem. Geol. 184, 231–254.
Reich, M., Parada, M.A., Palacios, C., Dietrich, A., Schultz, F., Lehmann, B., 2003. Adakite-like signature of late Miocene intrusions at the los Pelambres giant porphyry copper deposit in the Andes of Central Chile: metallogenic implications. Mineral. Deposita 38, 876–885.
Richards, J.P., 2003. Tectono-magmatic precursors for porphyry Cu–(Mo–Au) deposit formation. Econ. Geol. 98, 1515–1533.
Sengor, A.M.C., Natal'in, B.A., 1996. Paleotectonics of Asia: Fragments of Synthesis. In: Yin, A., Harrison, T.M. (Eds.), The Tectonic Evolution of Asia. Cambridge University Press, Cambridge, pp. 486–640.
Sharp, W.D., Clague, D.A., 2006. 50-Ma initiation of Hawaiian emperor bend records major change in Pacific plate motion. Science 313, 1281–1284.
Sillitoe, R.H., 2010. Porphyry copper systems. Econ. Geol. 105, 3–41.
Smith, A.D., 2007. A Plate Model for Jurassic to Recent Intraplate Volcanism in the Pacific Ocean Basin. In: Foulger, G.R., Jurdy, D.M. (Eds.), Plates, Plumes, and Planetary Processes. Geol. Soc. Am. Spec. Pap. Vol. 430, pp. 471–495.
So, C.S., Zhang, D.Q., Yun, S.T., Li, D.X., 1998. Alteration mineralization zoning and fluid inclusions of the high sulfidation epithermal Cu–Au mineralization at Zijinshan, Fujian province, China. Econ. Geol. 93, 961–980.
Sun, S.S., McDonough, W.F., 1989. Chemical and Isotopic Systematics of Oceanic Basalts: Implications for Mantle Composition and Processes. In: Saunders, A.D., Norry, M.J. (Eds.), Magmatism in the Ocean Basins: Geological Society 42. Special Publications, London, pp. 313–345.
Sun, W.D., Ding, X., Hu, Y.H., Li, X.H., 2007. The golden transformation of the cretaceous plate subduction in the west pacific. Earth Planet. Sci. Lett. 262, 533–542.
Sun, W.D., Huang, R.F., Li, H., Hu, Y.B., Zhang, C.C., Sun, S.J., Zhang, L.P., Ding, X., Li, C.Y., Zartman, R.E., Ling, M.X., 2015. Porphyry deposits and oxidized magmas. Ore Geol. Rev. 65, 97–131.
Tang, G.J., Wang, Q., Wyman, D.A., Li, Z.X., Zhao, Z.H., Yang, Y.H., 2012. Late carboniferous high $\varepsilon_{Nd}(t)$–$\varepsilon_{Hf}(t)$ granitoids, enclaves and dikes in western Junggar, NW China: ridge-subduction-related magmatism and crustal growth. Lithos 140, 86–102.
Trail, D., Watson, E.B., Tailby, N.D., 2011. The oxidation state of hadean magmas and implications for early Earth's atmosphere. Nature 480, 79–82.
Trail, D., Watson, E.B., Tailby, N.D., 2012. Ce and Eu anomalies in zircon as proxies for the oxidation state of magmas. Geochim. Cosmochim. Acta 97, 70–87.
Wang, C.H., Tang, J.X., Hou, K.J., Gao, Y.M., Chen, J.P., Hao, J.H., Ying, L.J., Zhang, Q.Z., Liu, Y.W., Fan, T., 2011. Hf isotopic characteristics of Yulong copper-molybdenum porphyry deposit in Tibet and their geological significance. Mineral Deposits 30, 292–304 (in Chinese with English abstract).
Wang, G.G., Ni, P., Yao, J., Wang, X.L., Zhao, K.D., Zhu, R.Z., Xu, Y.F., Pan, J.Y., Li, L., Zhang, Y.H., 2015. The link between subduction-modified lithosphere and the giant Dexing porphyry copper deposit, South China: constraints from high-Mg adakitic rocks. Ore Geol. Rev. 67, 109–126.
Wang, S.H., Pei, R.F., Zeng, X.H., Qiu, X.P., Wei, M., 2009. Metallogenic series and model of the Zijinshan mining field. Acta Geol. Sin. 25, 145–157 (in Chinese with English abstract).
Wang, Y., Xue, C., Wang, J., Peng, R., Yang, J., Zhang, F., Zhao, Y., 2014. Petrogenesis of magmatism in the Yandong region of eastern Tianshan, Xinjiang: geochemical, geochronological, and Hf isotope constraints. Int. Geol. Rev. 1–22 (ahead-of-print).
Wang, Y.J., Fan, W.M., Cawood, P.A., Li, S.Z., 2008. Sr-Nd-Pb isotopic constraints on multiple mantle domains for Mesozoic mafic rocks beneath the South China block. Lithos 106, 297–308.
Wang, Y.J., Fan, W.M., Zhang, G.W., Zhang, Y.H., 2013. Phanerozoic tectonics of the South China block: key observations and controversies. Gondwana Res. 23, 1274–1305.
Winchester, J.A., Floyd, P.A., 1977. Geochemical discrimination of different magma series and their differentiation products using immobile elements. Chem. Geol. 20, 325–343.
Wu, C., Chen, H.Y., Hollings, P., Xu, D.R., Liang, P., Han, J.S., Xiao, B., Cai, K.D., Liu, Z.J., Qi, Y.K., 2015. Magmatic sequences in the Halasu Cu Belt, NW China: trigger for the Paleozoic porphyry Cu mineralization in the Chinese Altay–east Junggar. Ore Geol. Rev. 71, 373–404.
Wu, L.Y., Hu, R.Z., Qi, Y.Q., Zhu, J.J., 2013. Zircon LA-ICP-MS U–Pb ages and geochemical characteristics of quartz syenite porphyry from Jintonghu deposit in Zijinshan ore field, Fujian Province, South China. Acta Petrol. Sin. 29, 4151–4166 (in Chinese with English abstract).
Yang, S.Y., Jiang, S.Y., Jiang, Y.H., Zhao, K.D., Fan, H.H., 2010. Zircon U–Pb geochronology, Hf isotopic composition and geological implications of the rhyodacite and rhyodacitic porphyry in the Xiangshan uranium ore field, Jiangxi Province, China. Sci. China Earth Sci. 53 (1), 1411–1426.
Yang, W.P., Zhang, Z.C., Zhou, G., Yan, S.H., He, L.X., Chen, B.L., 2005. Discovery of the Xileketehalasu porphyry copper deposit on the southern margin of the Altay copper metallogenic belt. Chin. Geol. 32, 107–114 (in Chinese with English abstract).
Yu, B., Pei, R.F., Qiu, X.P., Chen, J.H., Li, D.P., Zhang, W.H., Liu, W.Y., 2013. The evolution series of Mesozoic magmatic rocks in the Zijinshan Orefield, Fujian Province. Acta Geol. Sin. 34, 437–446 (in Chinese with English abstract).
Yuan, H.L., Gao, S., Liu, X.M., Li, H.M., Gunther, D., Wu, F.Y., 2004. Accurate U–Pb age and trace element determinations of zircon by laser ablation-inductively coupled plasma-mass spectrometry. Geostand. Geoanal. Res. 28, 353–370.
Zhang, D.Q., Li, D.X., Zhao, Y.M., Chen, J.H., Li, Z.L., Zhang, K.Y., 1991. The Zijinshan deposit: The first example of quartz-alunite type epithermal deposit in the continent of China. Geological Review 37 (6), 481–491.
Zhang, D.Q., Li, D.X., Zhao, Y.M., Wang, W.G., Gu, G.X., 1996. The Wuziqilong copper deposit: the deformed upper part of a porphyry copper deposit. Mineral Deposits 15, 109–122 (in Chinese with English abstract).
Zhang, D.Q., Li, D.X., Feng, C.Y., Dong, Y.J., 2001. The temporal and spatial framework of the Mesozoic magmatic system in Zijinshan area and its geological significance. Acta Geosci. Sin. 22, 403–408 (in Chinese with English abstract).
Zhang, D.Q., She, H.Q., Li, D.X., Feng, C.Y., 2003. The porphyry–epithermal metallogenic system in the Zijinshan region, Fujian province. Acta Geol. Sin. 77, 253–261 (in Chinese with English abstract).
Zhang, D.Q., Feng, C.Y., Li, D.X., She, H.Q., Dong, Y.J., 2005. The evolution of ore-forming fluid in the porphyry–epithermal metallogenic system of Zijinshan area. Acta Geosci. Sin. 26, 127–136 (in Chinese with English abstract).
Zhang, H., Ling, M.X., Liu, Y.L., Tu, X.L., Wang, F.Y., Li, C.Y., Liang, H.Y., Yang, X.Y., Arndt, N.T., Sun, W.D., 2013. High oxygen fugacity and slab melting linked to Cu mineralization: evidence from Dexing porphyry copper deposits, southeastern China. J. Geol. 121, 289–305.
Zhang, J.Z., 2013. Geology, exploration model and practice of Zijinshan ore concentrated area. Mineral Deposits 32, 757–766 (in Chinese with English abstract).
Zhao, Y., Xu, G., Zhang, S.H., Yang, Z.Y., Zhang, Y.Q., Hu, J.M., 2004. Yanshanian movement and conversion of tectonic regimes in East Asia. Earth Sci. Front. 11, 319–328 (in Chinese with English abstract).
Zhao, X.L., Mao, J.R., Chen, R., Xu, N.Z., Zeng, Q.T., Ye, H.M., 2007. Zircon SHRIMP age and geochemical characteristics of the Caixi pluton in southwestern Fujian province. Acta Petrol. Mineral. 26, 223–231 (in Chinese with English abstract).
Zhao, X.L., Mao, J.R., Chen, R., Xu, N.Z., 2008. SHRIMP zircon dating of the Zijinshan pluton in southwestern Fujian and its implications. Geol. China 35, 590–597 (in Chinese with English abstract).
Zhong, J., Chen, Y.J., Chen, J., Li, J., Qi, J.P., 2011. Fluid inclusion study of the Luoboling porphyry Cu–Mo deposit in the Zijinshan ore field, Fujian province. Acta Petrol. Sin. 27, 1410–1424 (in Chinese with English abstract).
Zhong, J., Chen, Y.J., Pirajno, F., Chen, J., Li, J., Qi, J.P., Li, N., 2014. Geology, geochronology, fluid inclusion and H–O isotope geochemistry of the Luoboling porphyry Cu–Mo deposit, Zijinshan Orefield, Fujian Province, China. Ore Geol. Rev. 57, 61–77.
Zhong, J., 2014. Temporal and Spatial Evolution of the Zijinshan Porphyry–Epithermal Magmatic and Mineralization System, Fujian Province. Peking University, Beijing (pH.D. Thesis).
Zhou, L.G., Xia, Q.X., Zheng, Y.F., Hu, Z., 2014. Polyphase growth of garnet in eclogite from the Hong'an orogen: constraints from garnet zoning and phase equilibrium. Lithos 206, 79–99.
Zhou, T.F., Wang, S.W., Fan, Y., Yuan, F., Zhang, D.Y., White, N.C., 2015. A review of the intracontinental porphyry deposits in the Middle–Lower Yangtze River valley metallogenic belt, eastern China. Ore Geol. Rev. 65, 433–456.
Zhou, X.M., Li, W.X., 2000. Origin of late Mesozoic igneous rocks in southeastern China: implications for lithosphere subduction and underplating of mafic magmas. Tectonophysics 326, 269–287.